2014

Synchrotron X-Ray Diffraction and Piezospectroscopy used for the Investigation of Individual Mechanical Effects from Environmental Contaminants and Oxide Layer Undulations in Thermal Barrier Coatings

Sanna Siddiqui
University of Central Florida, Sanna.Siddiqui@knights.ucf.edu

SYNCHROTRON X-RAY DIFFRACTION AND PIEZOSPECTROSCOPY USED FOR THE INVESTIGATION OF INDIVIDUAL MECHANICAL EFFECTS FROM ENVIRONMENTAL CONTAMINANTS AND OXIDE LAYER UNDULATIONS IN THERMAL BARRIER COATINGS

by

Sanna F. Siddiqui
B.S.A.E. University of Central Florida, 2012

A thesis submitted in partial fulfillment of the requirements
for the degree of Master of Science
in the Department of Mechanical and Aerospace Engineering
in the College of Engineering and Computer Science
at the University of Central Florida
Orlando, Florida

Summer Term
2014

Major Professor:
Seetha Raghavan

Abstract

The durability of Thermal Barrier Coatings (TBCs) used on the turbine blades of aircraft and power generation engines has been known to be affected by sand particle ingression comprised of Calcium-Magnesium-Alumina-Silicate (CMAS). Previous studies have shown that these effects present themselves through variations in the thermomechanical and thermochemical properties of the coating. This study investigated the impact of CMAS ingression on the Yttria Stabilized Zirconia Topcoat (YSZ) and Thermally Grown Oxide (TGO) strain in sprayed Thermal Barrier Coating (TBC) samples of varying porosity with and without CMAS ingression. In-Situ Synchrotron X-ray Diffraction measurements were taken on the sample under thermal loading conditions from which the YSZ and TGO peaks were identified and biaxial strain calculations were determined at high temperature. Quantitative strain results are presented for the YSZ and TGO during a thermal cycle. In-plane strain results for YSZ near the TGO interface for a complete thermal cycle are presented, for a 6% porous superdense sample with CMAS infiltration. The outcomes from this study can be used to understand the role of CMAS on the strain tolerance of the TBC coating.

It is well known that under engine operational conditions the development of the TGO layer, with large critical stresses, has been linked to failure of the coating. The growth of the TGO manifests as undulations in a series of peaks and troughs. Understanding the mechanics of the oxide layer at these locations provides significant information with re-

spect to the failure mechanisms of the TBC coating. This study investigated the stress at the peak and trough of a TGO undulation for a cycled Dense Vertically Cracked (DVC) plasma sprayed TBC sample through photo-luminescence (PL) spectroscopy. High resolution nanoscale stress maps were taken nondestructively in the undulation of the TGO. Preliminary results from first line mapping of TGO peak and trough scan, at a resolution of 200 nm, have shown a non-uniform TGO stress variation. The results obtained from this study can be used to understand the stress variation in the peak and trough of a DVC sample's TGO undulation and how it contributes to the life of the TBC coating.

This work is dedicated to my parents and sister for their love, encouragement and guidance which have inspired me to achieve my dreams.

Acknowledgments

I would like to express my appreciation foremost to my thesis chair and research advisor, Dr.Seetha Raghavan, for her guidance, motivation and support throughout the course of this project. I would also like to thank my committee members, Dr.Ali P. Gordon and Dr.Yuanli Bai, for their knowledgeable advice. I would like to express my gratitude to my professors, Dr.Challapalli Suryanarayana and Dr.Alain Kassab, for their motivation. I would like to thank Dr.Jonathan Almer and Dr.John Okasinski at Argonne National Laboratory (ANL) for their expert advice on XRD data analysis, providing the programs necessary for analysis and for their help during XRD data collection. I would like to acknowledge Dr.Li Li and Dr.Albert Feuerstein at Praxair Surface Technologies for providing the samples for these experiments. I would also like to thank Dr.Marion Bartsch and all our collaborators at the German Aerospace Center (DLR). I would like to also thank Dr.Laurene Tetard at the NanoScience Technology Center at the University of Central Florida for her help during data collection. Thank you to Stephen Sofronsky, Kevin Knipe, Albert Manero and all my colleagues at the University of Central Florida for their assistance and advice. This material is based upon work supported by the National Science Foundation Grant Nos.(CMMI 1125696) and (OISE 1157619), and German Science Foundation (DFG) Grant No.(SFB-TRR103), Project A3. This work is additionally based upon work supported by the National Science Foundation Graduate Research Fellowship Program under Grant No. (1144246). Use of the Advanced Photon Source, an Office of Science User Facility operated for the U.S. Department of Energy

(DOE) Office of Science by Argonne National Laboratory, was supported by the U.S. DOE under Contract No. DE-AC02-06CH11357.

TABLE OF CONTENTS

LIST OF FIGURES

LIST OF TABLES

CHAPTER 1
INTRODUCTION

1.1 Thermal Barrier Coatings (TBCs) Background

Thermal Barrier Coatings (TBCs) are ceramic coatings that are used on the turbine blades of power generation and aircraft gas turbine engines, which allow for higher engine operating temperatures and improved turbine efficiencies [17, 62, 24]. The motivation for studying the mechanics of these coatings over the past few decades has been to determine factors that can increase the durability and life of these coatings under engine operational conditions. Through this research, knowledge of the necessary design implications of the coating can be made, resulting in longer life of turbine blades and consequentially gas turbine engines.

The TBC system is comprised of four layers that include a ceramic top coat, a thermally grown alumina-oxide layer, a metallic bond coat (primarily Nickel-based) and a superalloy metal substrate (turbine blade) as shown in Figure 1.1. The ceramic topcoat, which is commonly 7 wt% Yttria Partially Stabilized (YSZ) Zirconia, acts as a thermal barrier between the turbine blade and hot gases in the combustion chamber of the engine, by reducing the amount of heat being transferred to the metal substrate. The thermally grown oxide (TGO) layer develops between the ceramic topcoat and metallic bondcoat (BC) upon thermal cycling of the coating. It has been linked to failure of the coating as a result of the development of large compressive stresses within the TGO due to large

thermal expansion mismatch between the layers. Growth of the TGO has been linked to the initiation of failure mechanisms within the coating such as spallation and delamination [25, 85, 16, 9, 38]. Finally, the metallic bondcoat acts as a bonding mechanism between the ceramic topcoat and the superalloy metal substrate. It additionally serves to prevent erosion and corrosion of the substrate.

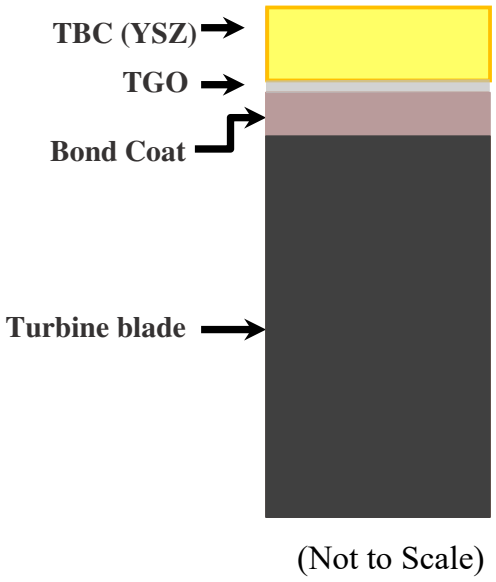

Figure 1.1: TBC System Schematic

TBC depositions have been achieved through plasma spray and electron beam physical vapor deposition (EB-PVD) methods. EB-PVD TBC coatings have a vertical columnar structure and are used primarily in aircraft engines. They are more durable because of their vertical columnar structure which allows for greater strain tolerance, but they have a higher thermal conductivity than plasma sprayed TBCs [63]. More recently,

advancements have been made in improving the strain tolerance of sprayed coatings for use in aircraft engines. This has been achieved with the development of dense vertically cracked (DVC) thermally sprayed TBCs, which are created by superimposing molten YSZ splats on the substrate and allowing them to solidify [76, 53]. Traditional plasma sprayed TBC coatings have a generally porous or splat type microstructure and are commonly used in power generation engines. As a result of their porous nature however, plasma sprayed TBC coatings are more susceptible to erosion. In general, the amount of TBC porosity in thermally sprayed samples can affect the level of erosion of the substrate [50]. As such, one aspect of this study uses samples with varying porosities (low density and superdense) to determine the thermo-mechanical effects of erosion within these samples. D-gun or detonation sprayed TBCs have a similar microstructure as plasma sprayed coatings, but are applied by controlled detonations of mixtures of powder and gases on the substrate. The superdense sample was D-gun sprayed whereas the low density samples were air plasma sprayed.

The motivation of this study is to understand how this erosive behavior, which is caused by the infiltration of environmental contaminants in the TBC coating, affects the mechanical properties of the layers of the coating. This is important because erosion is a common cause for failure in TBC coatings. In addition to characterizing the mechanical effects occurring within the TBC system as a result of erosion, this study further investigates the piezospectroscopic variation within TGO undulations. The motivation of this second study is to understand how variation in the local stresses within these TGO

undulations are linked to the initiation of other types of common failure mechanisms within the TBC coating including delamination and spallation. Overall, this work aims to study the mechanics within the layers of a TBC coating in order to further aid in the understanding of certain mechanisms leading to failure within TBCs, erosion and TGO undulations' development. An introduction on CMAS, which causes erosion, and TGO undulations are presented in the next sections.

1.2 Calcium Magnesium Alumina Silicate (CMAS)

Developments within the area of thermal barrier coatings (TBCs) used on the turbine blades of gas turbine engines have seen significant progress that have led to an increase in the operating temperature and efficiency of these engines. However, TBC coatings also need to endure harsh environments including the erosive effects of airborne contaminants infiltration on power generation and aircraft engine performances. This concern is especially seen in dusty environments such as deserts, sandy regions and underdeveloped flight runways where damage has been seen to occur in gas turbine engines [8], with studies also showing the effect of these dusty environments on turbofan and turboprop engines [22].

Early research has focused on understanding the effect of volcanic ash on the performance of aircraft engines. The effect of volcanic ash on reduced engine performance has been reported due to the melting of these deposits and subsequent blockage of flow

paths and cooling holes within the engine [43]. A comparative study by Dunn et al., for a technology program, has shown the effect of volcanic ash on varying types of engines and found that damage is dependent on the concentration and constituents of the material comprising the volcanic ash [21].

More recent studies have characterized the composition of the environmental contaminants that degrade TBC coatings. These contaminants have been found to be comprised of Calcium, Magnesium, Alumina and Silicate oxides (CMAS), through the use of differential thermal analysis [11]. In addition, a program has been developed to determine the major elements that comprise a CMAS system [26].

Understanding how the variation in TBC coating type (Plasma Sprayed or EB-PVD) can proliferate degradation is fundamental for improvements in coating design. A comparative study to determine the rate of errosion between plasma sprayed and EB-PVD TBC coatings when subjected to high velocity alumina and silica particles at room temperature and 910^oC, has shown that EB-PVD TBCs are more erosion resistant than plasma sprayed coatings [58]. In EB-PVD TBC coatings, it has also been shown that the minimum level of 4.8 mg/cm^2 of CMAS can initiate damage of the TBC [84]. Furthermore, it has been shown that the porous nature of the YSZ in sprayed coatings is susceptible to CMAS infiltration before chemical degradation of the coating begins, through Scanning Electron Microscopy and X-ray Diffraction [50].

CMAS studies have focused on the effect of these contaminants on both the thermochemical and thermomechanical degradation of thermal barrier coatings [49]. Melting of

such deposits was found to result in a phase change of the YSZ layer from tetragonal to monoclinic through energy dispersive x-ray spectroscopy, at a temperature of 1240^oC, leading to a loss in strain tolerance of the coating [48]. Thermochemical degradation of free-standing YSZ coatings subject to CMAS attack have also been examined [56, 27].

CMAS infiltration not only affects the chemical composition of the TBC coating, but leads to the initiation of failure mechanisms within the TBC coating. Accurate simulation of CMAS infiltration in a TBC coating is important to characterizing these failure mechanisms such as delamination. A study by Drexler et al. have presented thermal gradient cyclic testing of TBCs, in which CMAS is simultaneously ingested into the TBC coating, which has been able to more accurately map regions of delaminations in CMAS infiltrated samples [20]. The infiltration of CMAS has been found to lead to spallation of the TBC coating as a result of cold shock, which was identified through the sub-surface delamination characteristics within the penetrated TBC layers [55]. In addition to sub-surface delaminations, CMAS penetrated regions have been found to result in channel cracks and spallation [47]. Finite Element simulations have been used to further examine the energy release rates of these delamination mechanisms [14].

In addition to thermal barrier coatings, CMAS induced degradation is also of concern in environmental barrier coatings. CMAS infiltration has been found to initiate thermochemical and thermomechanical degradation of BSAS ($Ba_{1-x}Sr_xAl_2Si_2O_8$) environmental barrier coatings (EBC) [31, 34]. For example, a synchrotron x-ray diffraction, thermomechanical study has shown residual stress measurements in the BSAS topcoat

layer to be both non-uniform, and with a longer exposure time, increasingly compressive as a result of CMAS infiltration [34]. As studies on BSAS EBC's has shown, characterizing the effect of CMAS infiltration on the evolution of stress and strain is important in various types of environmental coatings. These studies allow for a more developed understanding of the effect of erosion on the mechanics of layered materials.

As has been shown, most CMAS studies have emphasized the thermochemical effects of CMAS infiltration on the TBC system. In addition, the thermomechanical studies presented have only analyzed the effect of CMAS infiltration on the initiation of failure mechanisms in the coating such as delamination and spallation. However, it is also important to understand how the mechanics of the TBC system may change as a result of CMAS infiltration, in order to completely define the thermomechanical changes experienced by the coating. The focus of this study is to portray these thermomechanical changes experienced by sprayed TBC coatings as a result of CMAS infiltration, under in-situ high temperature conditions.

The importance of in-situ studies on TBCs lies in providing not only the mechanics of the coating layers under realistic turbine operational conditions, but performance and life predictions of the coating [19, 71, 45]. In-situ studies are necessary to provide realistic strain and stress values endured by the coating at each stage of the loading conditions, which ultimately can lead to improvements to the design of these coatings. For example, in-situ experimentation has shown that under thermal and mechanical loading conditions, the TGO layer briefly experiences an in-plane tensile stress for dogbone TBC

samples [18]. This result is important because the TGO stress is generally found to be highly compressive, and tensile stresses are expected to result in initiation of damage. Furthermore, measurement techniques have been found to aid understanding of the mechanics of TBCs on cylindrical samples, which are representative of turbine blade geometry, under in-situ conditions [71]. By simulating similar operational conditions, the effect of CMAS on the TBC coatings can be more accurately predicted and understood, especially under dynamic conditions such as ramp up and ramp down. Furthermore, the findings from in-situ studies can allow for more accurate finite element (FE) simulations of both the thermochemical and thermomechanical changes observed in the TBC system as a result of CMAS infiltration. This will be possible because realistic experimental strain data will be available to validate FE simulation results.

Chapter 2 presents X-ray diffraction theory and the method for strain determination in these CMAS in-situ experiments. The experimental details and results obtained from these experiments are presented in Chapters 2 and 3.

1.3 Thermally Grown Oxide (TGO) Undulations

It is well known that under normal operating thermal loading conditions in power generation and aircraft engines, thermal barrier coatings develop a thermally grown oxide (TGO) layer as a result of oxidation of the bondcoat layer. This TGO growth occurs in the form of undulations and the critical stresses that develop within this layer are

a result of thermal expansion mismatch between the layers of the TBC coating. Understanding the variation of local stresses within these TGO undulations can provide significant information in predicting the onset of failure mechanisms within the TBC coating which can include spallation, delamination and buckling [23]. A few reasons for instability in this interface region has included non-uniform undulation geometry and thermal cycling [42, 40, 41]. Assessment of the regions where damage has occured has been shown by the broadening of photo-luminescence peaks near the damage region [64]. Air plasma sprayed samples have also shown crack formation as a result of TGO growth due to thermal cycling [13].

High resolution measurements of these critical stresses are important to accurately predict the performance of the TBC coatings. A study by T.Tomimatsu et al. has shown the local stress variation in the TGO layer through near-field optical microscopy at a resolution of 400 nm, for an EB-PVD 7 wt% YSZ TBC coating initially subjected to 20 hours of thermal exposure at 1100^oC [82]. This study found that the variation within the TGO undulation ranged from -0.8 GPa to -1.6 GPa, with the largest compressive stress occurring near the bondcoat [82]. Micro-luminescence spectroscopy has also been used to capture the stress variation in two types of TGO undulations, thickness imperfections and a uniform undulation on a cross section [81]. This study was done on an EB-PVD 7 wt% YSZ TBC coating initially subjected to 100 hours of thermal exposure at 1100^oC and showed that the stress near the TGO and bondcoat interface was higher for a uniform undulation than for the thickness imperfections [81]. Photo-luminescence measurements

from EB-PVD TBCs has also shown two varying residual stresses in intact and damaged locations within the TGO [69].

The variation in the stress in TGO undulations has also been previously studied using finite element simulation (FEM). Delamination failure mechanisms between the topcoat and TGO as a result of these critical stresses have been previously simulated as well as buckling and spallation failure near the TGO and bondcoat interface [10, 9]. Other FEM models have been used to understand the effect of TGO creep on stress in the peaks and troughs which yielded compressive and tensile stresses respectively [68].

Destructive testing methods such as indentation tests have also been used to determine the stresses within the TGO layer. Luminescence spectroscopy was used to measure the stress variation in the TGO layer of a Rockwell indented EB-PVD TBC coating in which the TGO stress was shown to vary in the delaminated area from 1.2 GPa to 3.2 GPa, the indenter area from 0 GPa to 1 GPa and in the area far from the indenter in the range of 4.2 GPa [75]. Another study analyzed the effect of thermal exposure and cyclic indentation on TGO residual stress and found that these stresses were affected by the damage caused by indentation [87].

Characterizing the stress variation in the topcoat YSZ layer has also been of interest, in order to understand how the local stress varies from the top of the YSZ layer to the YSZ and TGO interface. One such study used Raman spectroscopy to analyze the peak shift and stress in the topcoat layer for an EB-PVD 7 wt% YSZ TBC coating with a thickness of 700 μm; and showed that the YSZ peak shift is large near the interface and

there is a compressive stress near the interface [80]. Further work by M. Tanaka et al. measured the residual stress in an EB-PVD 4 wt% YSZ TBC coating with a thickness of 200 μm through micro-Raman spectroscopy which was found to be compressive through the TBC thickness [74].

As has been shown, most studies have analyzed or simulated TGO stress variation in EB-PVD TBC samples, both destructively and nondestructively. The focus of this study is to obtain high resolution stress measurements nondestructively, in the range of 200 nm, within a TGO undulation of a cycled dense vertically cracked (DVC) sprayed TBC sample, in order to quantify the stress variations as well as to understand and relate the geometry of the undulations with these localized stress variations. This study further aims to characterize TGO stress near the topcoat and bondcoat, to probe interface regions where failure initiates at a much more resolved scale. DVC sprayed TBC coatings are designed such that the topcoat contains uniform vertical cracks which increases the strain tolerance of sprayed coatings, enabling them to have increased durability [76]. As such, characterization of the local stress variations at the interface at high resolution, which has been possible because of the advancements in instrument technology, will further establish the durability level of DVC sprayed TBC coatings.

Piezospectroscopy theory and the method for stress determination in these experiments are presented in Chapter 2. The experimental details and results obtained from these experiments are presented in Chapter 4.

CHAPTER 2
XRD MEASUREMENTS AND PIEZOSPECTROSCOPY

2.1 Synchrotron X-Ray Diffraction Theory (XRD)

X-ray diffraction (XRD) as shown in Figure 2.1, is a common technique used to characterize various types of materials including material properties such as texturing and phase changes within a material, as well as their mechanical properties such as strain and stress determination. The technique is based upon Bragg's Law which is given by Equation 2.1, in which an X-ray beam of wavelength (λ) is incident at an angle (θ) on the crystallographic planes that make up the material [59, 36, 35]. (θ) is also called the Bragg angle. The order of reflection (n), of the x-ray beam is normally set to a value of n=1. Each crystallographic plane is separated by a distance (d), also known as the d-spacing of the material, which is specific to the (hkl) Miller indices of that lattice plane. The angle at which the X-ray beam is incident on the crystallographic plane is the same angle at which it diffracts. Upon diffraction, a Debye-Scherrer ring is formed on the area detector which presents the diffracted intensity of the grains or crystals that comprise the material [6]. For a single crystal, X-ray diffraction will result in two diffracted intensity spots, one representing the incident of the beam and one representing the diffraction of the beam. Alternatively, for a polycrystalline material, the X-ray beam will diffract in several different directions for each grain, resulting in diffraction rings with multiple diffracted intensity spots [59]. In a polycrystalline material, grains are also arranged in varying orientations which upon beam diffraction results in diffracted intensity spots

filling the 2D diffraction ring. Every spot on a diffraction ring represents the diffracted X-ray beam [36].

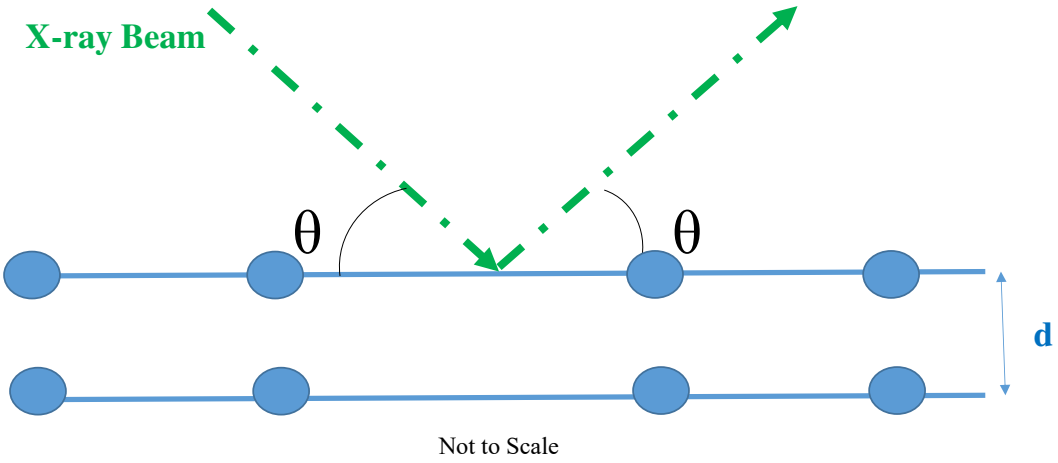

Figure 2.1: X-ray Diffraction Process as explained by Bragg's Law

$$n\lambda = 2 \cdot d \sin(\theta) \tag{2.1}$$

Most X-ray diffractometers are 1D and based upon the reflection geometry mode. XRD diffractometers based on the reflection geometry mode have certain limitations to them that includes minimal diffracted peak collection and X-ray penetration depth. However, the use of high energy synchrotron 2D X-ray diffraction, in which most are based upon the transmission geometry mode as in this study, has the advantage that it allows for the collection of several crystallographic planes with one exposure on a 2D area detector [5]. Most importantly, 2D X-ray diffraction has the advantage that it allows

for a collection of diffracted material peaks at varying sample orientations without the necessity of tilting the sample as in reflection geometry mode [6].

2.2 Bi-Axial Strain Determination Through XRD

Thermal Barrier Coatings are considered thin films. The stress (σ_{ij}) and strain (ε_{kl}) tensors describing this layered system can be simplified to a bi-axial state of stress for an isotropic material, in which the stress σ_{33} is assumed to be zero [5]. For strain and stress calculation from X-ray diffracted data, there are three coordinate systems that are considered: the laboratory coordinate system, the sample coordinate system and the crystallophysical coordinate system [46]. The crystallophysical coordinate system is used in defining the elastic constants (C_{ijkl}) for single crystals [46]. These elastic constants can be determined by the Reuss, Voigt or Kröner-Eshelby models [57]. In this study, the Reuss model is used because it assumes that the strain and stress tensors are equivalent in the sample coordinate system [5]. The elastic constants are used to calculate the X-ray elastic constants (S1 and (S2/2)) specific for each (hkl) lattice plane. In these experiments, the X-ray elastic constants were determined in the same manner, through the use of the DECcalc software [54]. Generalized Hooke's Law as shown in Equation 2.2 is used to determine the stress tensor σ_{ij}. In addition, Equation 2.3 is used to determine the strain tensor ε_{ij} from the elastic compliance s_{ijkl}.

$$\sigma_{ij} = C_{ijkl} \cdot \varepsilon_{kl} \tag{2.2}$$

$$\varepsilon_{ij} = s_{ijkl} \cdot \sigma_{kl} \tag{2.3}$$

The laboratory coordinate system (L_i) is fixed to the detector, whereas the sample coordinate system is fixed to the sample (S_i). The angles relating these two systems are the tilt angle (ψ) and the sample rotation (ϕ) [5]. The tilt angle (ψ) is used to relate the normal to the sample (S_3), to the detector normal (L_3). In X-ray diffraction reflection mode, tilting of the sample is with respect to a fixed detector direction. However in X-ray diffraction transmission mode, tilting of the sample is with respect to a fixed sample direction. The X-ray diffraction experiments presented here have used transmission mode. The tilt angle (ψ) can be determined from the detector azimuth angle (η) and Bragg's angle (θ_b) as shown in Equation 3.2, which applies for an η value between 0 and 90 degrees [5].

In order to determine the strain at any azimuthal angle, Equation 2.4 can be used, which calculates the change in d-spacing of a specific lattice plane ($d_\eta - d_0$) to the unstrained d-spacing of that lattice plane (d_0) [78]. Additionally, the diffraction ring radii for the unstrained (r_0) and strained (r_η) lattice plane can be used in the determination of strain at any azimuthal angle as shown in Equation 2.5 [5]. To determine the unstrained azimuthal angle, the tilt angle at which the strain is zero (ψ^*) must first be determined.

This can be found using Equation 3.1, which uses the X-ray elastic constants S1 and (S2/2) specific to each crystallographic plane, or Equation 2.6 which uses the Poisson's ratio specific to each crystallographic plane [5, 35]. After determining ψ^*, the unstrained azimuthal angle η^* can be determined from Equation 3.2. This unstrained azimuthal angle can be used in determining the unstrained radius (r_0) for strain calculation, as was done in this study. Details regarding the calculations are presented further in Section 3.3.1.

$$\varepsilon_\eta = (d_\eta - d_0)/d_0 \tag{2.4}$$

$$\varepsilon_\eta = (r_0 - r_\eta)/r_0 \tag{2.5}$$

$$sin^2(\psi^*) = 2(\nu_{hkl})/(1 + (\nu_{hkl})) \tag{2.6}$$

The Matlab program designed to determine the strain values for these experiments was provided by Dr. J. Almer at the 1-ID Beamline at Argonne National Laboratory and uses a Pseudo-Voigt function. This program azimuthally bins and radially integrates the diffracted data around the 2D diffraction ring to obtain an average strain value of the peak being analyzed. The calibration of the 2D detector was achieved using cerium dioxide powder in order to properly align the detector before data collection, in which the calibration parameters were determined using the Fit2D program [32, 33]. An example of

the resulting diffraction rings, lineout plot of the intensity of the diffracted peaks versus d-spacing, and radial plot produced by the program is shown in Figure 2.2. The radial plot can be used to qualitatively determine the presence of strain in different peaks by the presence of a double bell curve, which further illustrates that the layers are experiencing strain due to the external load. Under load, these Debye-Scherrer rings are seen to be elliptical.

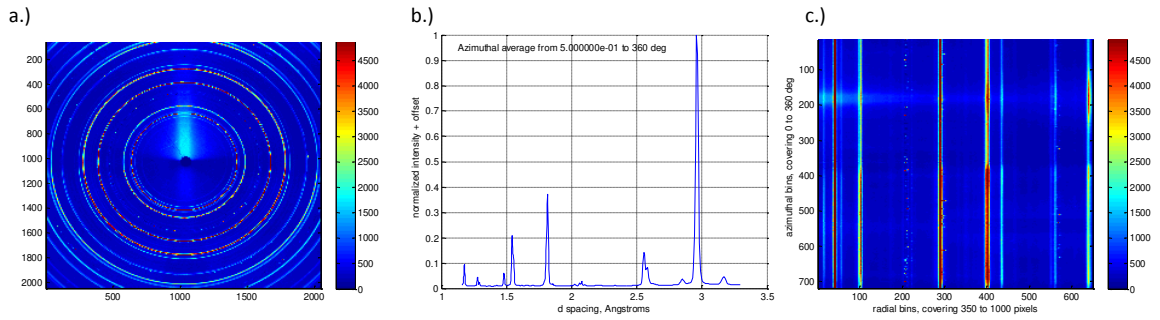

Figure 2.2: Plots for a Low density plasma sprayed TBC CMAS Sample produced in the Matlab Strain Program: a.) 2D Diffraction Rings b.) Lineout plot c.) Radial Plot

In addition, the peak of the material to be fitted must be inputted into the Matlab program. To achieve this, the peak must be identified correctly. This can be achieved using the JCPDS database provided International Centre for Diffraction Data, which provides detailed information on the d-spacing and intensity of the peaks for various materials. In this study, the peaks for 7 wt.% YSZ and Al_2O_3 TGO were identified using the JCPDS: 01-070-4430 and JCPDS: 00-042-1468, [3] and [2] respectively. It is important to note that YSZ Peak (101) at a d-spacing of 2.96 Å is at the same d-spacing

as ZrO_2 Peak (111), therefore this peak is commonly referred to as YSZ (111), as it is in the analysis of the experiments presented here. JCPDS: 00-017-0923 was used for ZrO_2 peak identification [4].This program also takes into account temperature correction of the lattice parameters (a) and (c) for each layer, because peak shifting can occur as a result of temperature variation.

2.3 XRD Measurement Techniques for CMAS Circular Disk Samples

Preliminary XRD experimentation of the CMAS Circular Disk samples presented in Chapter 3 of this study proved to be difficult because of the low diffraction volume intensity of the TGO layer captured during a single scan. This was due to the large diffraction volume of the sample, that the X-ray beam had to pass through before diffracting. The thick YSZ layer of these coatings also prevented the TGO layer from being captured. To counteract this problem, the samples were cut into semi-circular and rectangular geometries as shown in Figure 2.3. This study determined strain results from the diffracted rings of semi-circular cut samples. Such a geometry was successful because it resulted in higher TGO diffraction intensities which could yield bi-axial strain results within this layer.

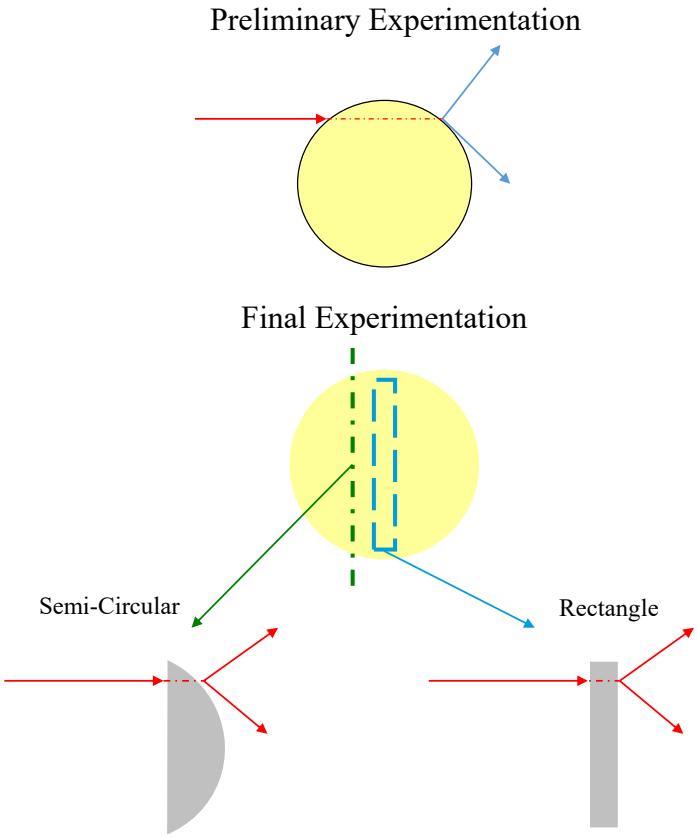

Figure 2.3: CMAS Sample Preliminary and Final Geometry to facilitate XRD Data Collection

2.4 Previous Study: XRD Measurement Techniques for Cylindrical TBC Specimens

The motivation for this previous study was to determine in-situ synchrotron X-ray diffraction techniques to effectively measure strain within the layers of a hollow cylindrical

EB-PVD TBC sample under realistic thermal gradient and mechanical loading testing conditions. This section presents two techniques and the individual benefits of both techniques as well as the difficulties of XRD data collection associated with each technique. These techniques provide the methods necessary for future XRD studies on realistic cylindrical geometries, simulating turbine blade geometry.

2.4.1 Experimental Details

In-situ synchrotron X-ray diffraction measurements were taken on a hollow EB-PVD thermal barrier coated (TBC) cylindrical sample with an inner diameter of 4 mm and an outer diameter of 8 mm, at the 1-ID-Beamline at the Advanced Photon Source in Argonne National Laboratory. The sample consisted of 7-8 wt.% Yttria-Stabilized Zirconia (YSZ) ceramic topcoat with a thickness of 211+/- 4 μm, an Al_2O_3 TGO layer thickness of approximately 0.3 μm, and a NiCoCrAlY metallic bond coat with a thickness of 118 +/- 4 μm. The coating was applied on an IN100 substrate and the sample was prepared at the German Aerospace Center (DLR) [71].

2.4.2 Effect of Synchrotron XRD Parameters on Intensity

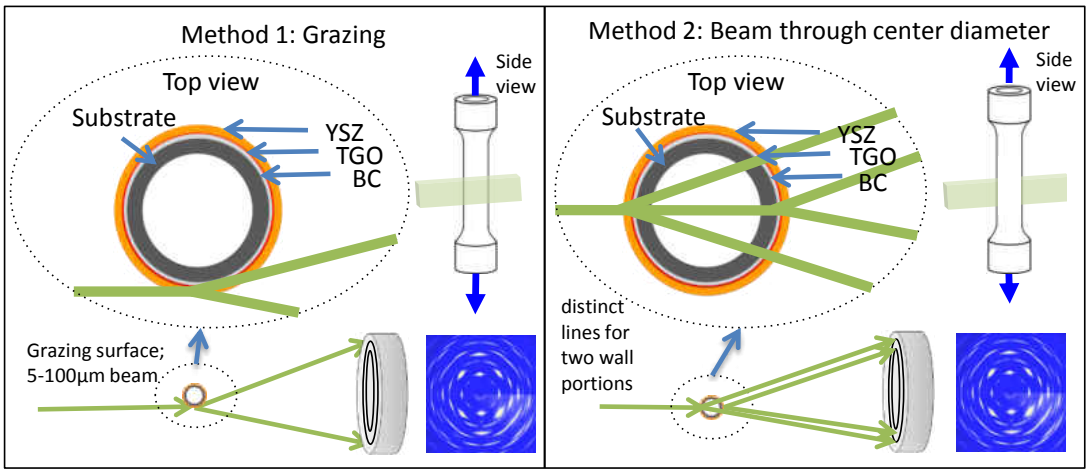

Figure 2.4: Method 1: Grazing surface from 5-100 μm. 2D detector measures axial and radial components of stress. By moving the sample into the beam, information from different layers is collected. Method 2: Direct Transmission along the center line. 2D detector measures wall-thickness-averaged axial and circumferential components. [71]

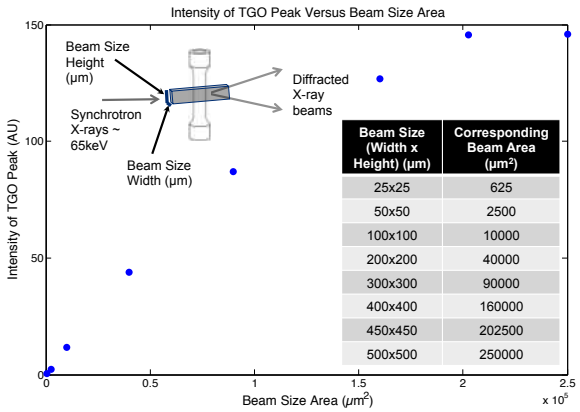

Figure 2.5: Detected TGO intensity with varying Beam Size Area [71]

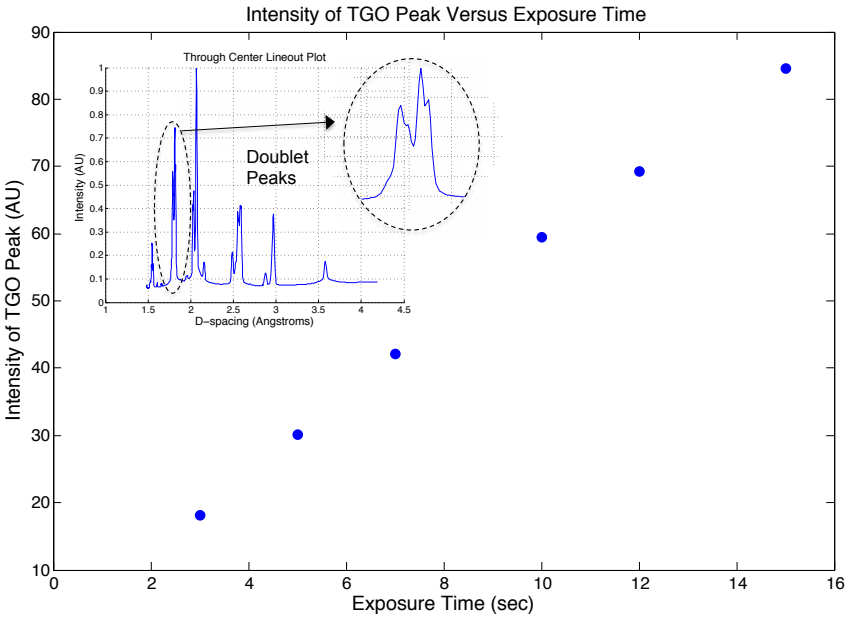

Figure 2.6: Detected TGO intensity with varying Exposure Time [71]

Measurement techniques were found to aid understanding of the mechanics of TBCs on cylindrical samples under in-situ conditions. These techniques are presented in Figure 2.4. In Method 1, the X-ray beam grazes the edge of the sample, from which axial and radial components of strain can be measured within the layers of the thermal barrier coating. In Method 2, the X-ray beam passes through the center of the sample, from which axial and circumferential strain components can be measured. The effectiveness of these two methods in obtaining strain measurements within the TBC layers was analyzed. Method 1 was found to yield varying phases of the YSZ, TGO and Bondcoat. In Method 2, the effect of varying XRD synchrotron parameters (beam size and exposure time) on the intensity of the TGO peak (116) was analyzed due to the low diffraction volume

of the TGO for the through center method, in order to obtain sufficient intensity for strain measurements. At a constant exposure time of 0.5 s and frame count of 1 frame, the beam size was varied as shown in Figure 2.5. The resulting intensity of TGO peak (116) with varying beam size is shown in Figure 2.5. It is important to note here that the highest intensity of the TGO peak was not obtained at the largest beam area. As evident in Figure 2.5, the highest intensity of the TGO peak was obtained at a beam size of (450 X 450) $\mu m * \mu m$, after which the curve is noticed to plateau. In addition, at a constant beam size of (40 X 300) $\mu m * \mu m$, the exposure time was varied to 3, 5, 7, 10, 12, and 15 s. The effect of varying exposure time on the intensity of TGO peak (116) is shown in Figure 2.6 respectively. The relationship between the intensity of the TGO peak (116) and varying exposure time displayed a linear trend, with a correlation coefficient of $R^2 = 0.9983$. Furthermore, an increase in TGO intensity is noted with an increase in exposure time [71].

One of the challenges in applying Method 1 for strain measurements are the presence of doublet peaks acquired, which result due to the beam passing through each coating layer twice as shown in Figure 2.4. The presence of these doublet peaks requires additional analysis techniques in order to fit a strain curve. However, the use of the through center method is effective in yielding sufficient intensities to obtain axial and circumferential components of strain. From the earlier described grazing results, clear peak position acquisition for various peaks of each layer provide strain components in both axial and radial directions. These results show the ability of both these methods, with

the appropriate parameters, to measure multiple locations on the curvature in order to yield the full strain tensor required for in-situ strain determination [71].[1]

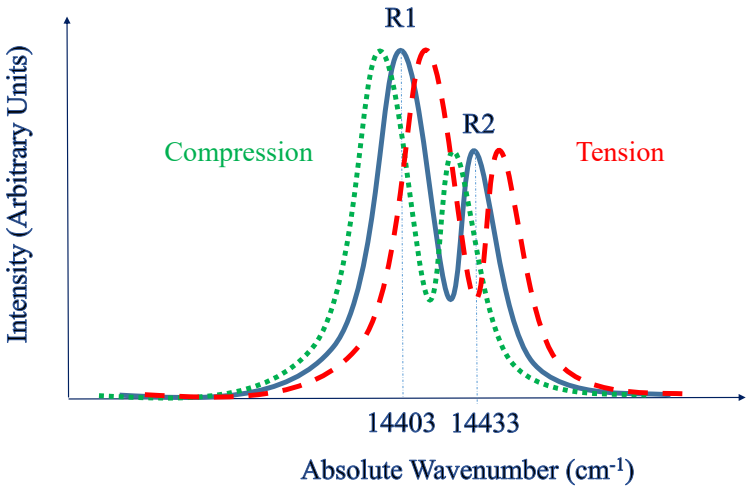

Figure 2.7: Schematic of R-line peak shift under compressive and tensile stress

2.5 Piezospectroscopy Theory

Photoluminescene Spectroscopy is a technique commonly used to assess damaged regions and nondestructively measure stress within several materials, including the alumina oxide TGO layer of TBCs [28, 16, 67, 51, 64, 69, 15, 61, 60, 73]. Piezospectroscopy is the study of stress determination from the shift of spectral R-line peaks. The R-lines (R1 and R2), which are characteristic of α-alumina, are a result of laser excitation that causes the

[1]Figures 2.4, 2.5, 2.6 and Excerpts in section entitled "Previous Study: XRD Measurement Techniques for Cylindrical TBC Specimens," are from my publication: S. F. Siddiqui et al. Synchrotron X-ray measurement techniques for thermal barrier coated cylindrical samples under thermal gradients. Review of Scientific Instruments, 84:083904, 2013.

chromium (Cr^{3+}) ions within alumina to transition from a high energy state to ground state. The absolute wavenumber positions for R1=14403 cm^{-1} and for R2=14433 cm^{-1}. The shifting of these R-lines indicate the presence of stress as shown in Figure 2.7, with compressive stress occurring as a result of the peaks shifting left and tensile stress occurring as a result of the peaks shifting right from their absolute wavenumber positions. The frequency shift of these R-lines can be related to the stress tensor as described by Equation 2.7 [30]. In this equation, $\Delta\nu$ is the frequency shift of the spectral peaks, π_{ij} is a 2nd order tensor of the Piezospectroscopic (PS) coefficients and σ_{ij} is the stress tensor in the crystal reference frame. Equation 2.7 was further simplified to Equation 2.8, which shows that the frequency shift $\overline{\Delta\nu}$ for a polycrystalline material only depends upon the trace of the stress tensor $(\sigma_{11} + \sigma_{22} + \sigma_{33})$ [52].

$$\Delta\nu = \pi_{ij}\sigma_{ij} \tag{2.7}$$

$$\overline{\Delta\nu} = 1/3(\pi_{11} + \pi_{22} + \pi_{33})(\sigma_{11} + \sigma_{22} + \sigma_{33}) \tag{2.8}$$

The R1 and R2 PS coefficients along the principal crystallographic and shear directions on a 0.05 wt.% ruby was determined by He and Clarke [37] to be described by Equations 2.9 and 2.10. Summing these PS coefficients as shown in Equation 2.8, the PS coefficients for R1 and R2 are $\pi_{R1} = 7.59\ cm^{-1} * GPa^{-1}$ and $\pi_{R2} = 7.61\ cm^{-1} * GPa^{-1}$ respectively [37, 61]. Assuming biaxial stress state conditions with $\sigma_{11} = \sigma_{22} = \sigma$ and

$\sigma_{33} = 0$, Equation 2.11 was used in this study for TGO stress determination caused by the shifting of R1 and R2 peaks [61].

$$\Delta\nu_{R1} = 2.56(\sigma_{11}) + 3.50(\sigma_{22}) + 1.53(\sigma_{33}) \tag{2.9}$$

$$\Delta\nu_{R2} = 2.65(\sigma_{11}) + 2.80(\sigma_{22}) + 2.16(\sigma_{33}) \tag{2.10}$$

$$\Delta\nu = 2/3(\pi_{ij})(\sigma) \tag{2.11}$$

In order to accurately determine the spectral peak position for stress calculation, it is necessary to deconvolute and curve fit the R-line peaks. To achieve this, certain parameters of the R-line peaks must be taken into consideration that reflect both theoretical and experimental observations of the physical behavior of these peaks. This includes the R1 and R2 peak positions, intensity ratio, full width at half maximum (FWHM), area of the peaks, separation of peaks and the peak shape defined by the Gaussian and Lorentzian shape factors [69, 61, 65]. This study uses a genetic algorithm based Matlab code for global optimization in the fitting procedure, which uses two Pseudo-Voigt functions for R1 and R2 fitting, taking into consideration the important physical behavior of these peaks mentioned earlier [65]. An example of the deconvoluted fits using the program can be seen in Figure 2.8, which was taken on a TBC coated cylindrical sample.

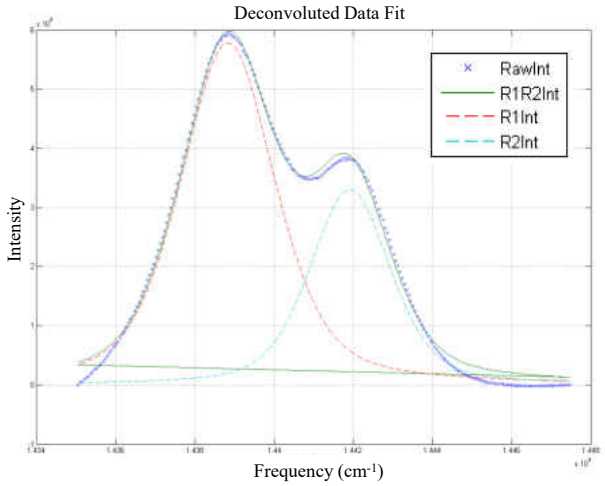

Figure 2.8: Example of Deconvoluted Fits within GA Program

CHAPTER 3
EFFECT OF CMAS ON STRAIN IN LAYERS OF THE TBC

3.1 Introduction

The purpose of this study was to further understand the role that CMAS plays on the strain within both the YSZ and TGO layers of both low density and superdense thermally sprayed CMAS coated TBC samples. This was achieved through in-situ synchrotron X-ray diffraction measurements taken under thermal loading conditions. This study aims to provide an understanding of the role of CMAS in affecting the strain at the interface, since this region is critical to initiation of failure mechanisms of the coating. The results presented quantify the in-plane strain in the YSZ and TGO layers for samples with CMAS infiltration of varying YSZ porosities as well as for a control sample without CMAS. The outcomes from this experiment can be used to further understand the role of CMAS in affecting the strain tolerance of the TBC under real world conditions and is relevant to future studies pertaining to ingression of volcanic ash and fuel impurities.

3.2 Materials and Methods

3.2.1 Sample Preparation

This section will highlight the thermally sprayed samples used in this study including the sample dimensions, process of CMAS infiltration and properties of the TBC coating

applied on each sample. It will further present details on the concentration of CMAS within each sample.

3.2.1.1 Low density TBC Samples

In order to analyze the effect of CMAS on strain within the TGO and YSZ layers, in-situ synchrotron X-ray diffraction measurements were taken on two low density deposition, air plasma sprayed TBC samples in which one was coated with CMAS. Infiltration of the CMAS was achieved through a 60 second flame burner process using a CMAS cement tape with a concentration level of 13 mg/ccm [50]. The composition of the CMAS infiltrated within the sample is presented in Table 3.2. These low density deposition samples had a porosity of 15%. Both samples were initially circular disks with the TBC coating applied on a Hast-X substrate that were waterjet cut into semi-circular disks to facilitate XRD data collection on the TGO layer. The CMAS coated sample had a diameter of 25.5 mm and a thickness of 4.5 mm. The control sample without CMAS infiltration had a diameter of 25.6 mm and a thickness of 4.0 mm. Details on the thickness of the 7 wt.% YSZ and Ni alloy bondcoat of the TBC coating for both samples are presented in Table 3.1.

Table 3.1: Low density with and without CMAS sample properties

Deposition (APS)	YSZ Thickness	Bond Coat Thickness	Substrate
Low density	635 μm (25 mils)	152.4 μm (6 mils)	Hast-X

Table 3.2: Composition of CMAS in Low density and Superdense CMAS samples

CaO (wt.%)	MgO (wt.%)	Al_2O_3 (wt.%)	SiO_2 (wt.%)	$Fe_2O_3(wt.\%)$
32.9	7.23	12.68	46.71	0.41

3.2.1.2 Superdense TBC Sample

In-situ synchrotron X-ray diffraction measurements were also taken on a superdense deposition, detonation sprayed TBC sample infiltrated with CMAS. Infiltration of the CMAS was achieved through a 60 second flame burner process using a CMAS cement tape with a concentration level of 12.61 mg/ccm [50]. This superdense deposition sample had a YSZ porosity of 6% and the composition of the CMAS infiltrated within the sample is presented in Table 3.2. The 7 wt.% YSZ TBC coating was applied on a MarM509 substrate and had a thickness of 381 μm. This sample was a semi-circular sample that had a diameter of 25 mm and a thickness of 3.8 mm.

3.2.2 Experimental Setup

3.2.2.1 Low density with and without CMAS Samples' Experimental Setup

The experimental setup of both samples at Argonne National Laboratory was as shown in Figure 3.1. Each sample was placed on an alumina sample holder with the X-ray beam passing parallel to the sample. 2D X-ray diffraction (XRD) room temperature measurements were taken on both samples before cycling, using a beam size of (300x30) $\mu m * \mu m$ (width x height), and an exposure time of 1 second at 10 frames. At ramp up, high temperature, ramp down and room temperature after cycling, the beam size was (300x40) $\mu m * \mu m$ (width x height) for the low density with CMAS sample. For the low density TBC sample with CMAS deposition, the X-ray beam energy was 86 keV with a sample to detector distance of 1601 mm. For the control sample without CMAS deposition, the X-ray beam energy was 65 keV with a sample to detector distance of 1539 mm. The low density CMAS sample was subjected to an 80 minute thermal cycle which included a 20 minute ramp up to 1121^oC, a 40 minute isothermal hold at 1121^oC and a 20 minute ramp down to room temperature. XRD measurements were taken by scanning through the thickness of the sample from the top surface to the substrate. These measurements were taken at each stage of the cycle from which the strain in TGO peak (116) and YSZ peak (111) were determined. Two k-type thermocouples were positioned on either side of the semi-circular sample to obtain temperature readings during the

80 minute thermal cycle. XRD room temperature measurements were obtained on the control low density sample without CMAS deposition.

3.2.2.2 Superdense TBC Sample Experimental Setup

The experimental setup and procedure of the Superdense TBC sample with CMAS was also as shown in Figure 3.1. 2D X-ray diffraction (XRD) room temperature, ramp up, high temperature and ramp down measurements were taken on the sample, using a beam size of (300x30) $\mu m * \mu m$ (width x height), and an exposure time of 1 second at 10 frames. The X-ray beam energy was also 86 keV with a sample to detector distance of 1601 mm, and this sample was subjected to the same thermal cycle as the low density TBC sample with CMAS. However, it is important to note that in preliminary experimentation, the Superdense TBC sample with CMAS was subjected to another 80 minute thermal cycle. Therefore, it has been subjected to 2 thermal cycles, one in the current experiment and one in previous preliminary experimentations. XRD measurements were taken at each stage of the cycle from which the strain in YSZ peak (111) was determined.

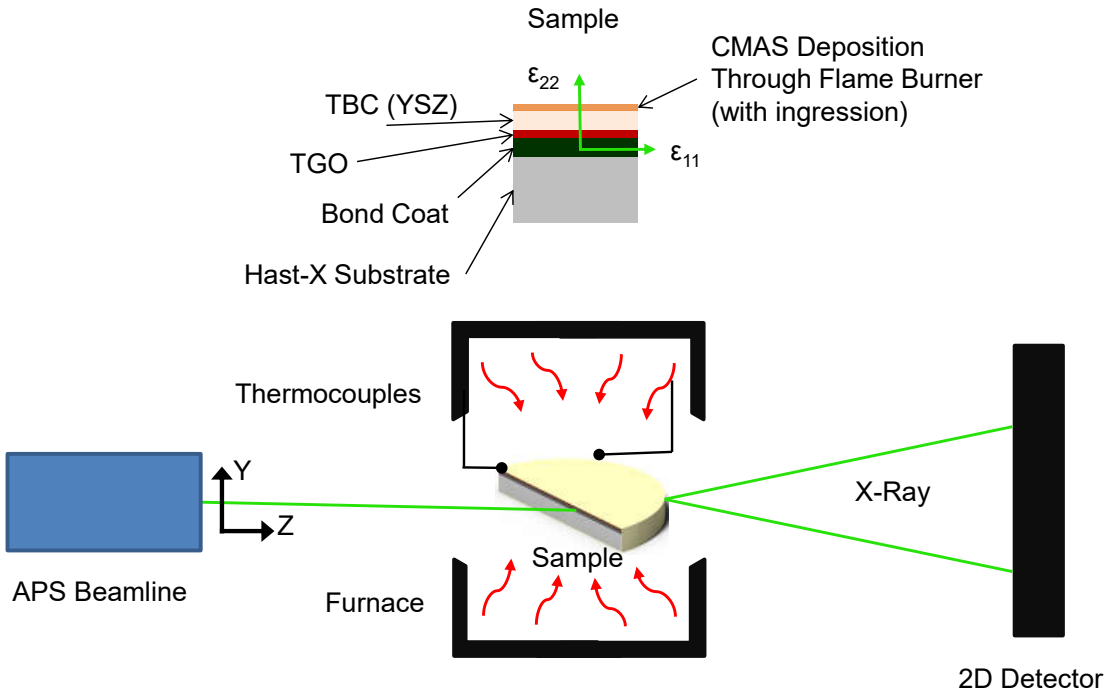

Figure 3.1: Schematic of X-ray Diffraction Experimental Setup of Sample (Top View) at Argonne National Laboratory (Not to Scale). ε_{11} is the in-plane strain and ε_{22} is the out-of-plane strain.

3.3 Low density with and without CMAS Sample Strain Results

3.3.1 Determination of Strain Free Radius

Studies have presented the process for determining the strain free radius or d-spacing for biaxial strain calculations. However in order to determine this strain free radius, the

single-crystal X-ray elastic constants (XEC) must first be determined from the material's elastic constants [57]. One of the most prominent approaches to determine the elastic constants is through the use of the Voigt, Reuss or Kröner-Eshelby models. The single crystal elastic constants in this study were determined through the Reuss model because it determines the strain tensor for varying crystallographic planes [12]. In this study, the Reuss X-ray elastic constants S1 and (S2/2) for the TGO and YSZ peaks were determined as well as the Poisson's ratio through use of the DECcalc software [54]. For TGO Peak (116) and YSZ Peak (111), the X-ray elastic constants S1 and (S2/2) computed through the DECcalc software are presented in Table 3.3. To determine the X-ray elastic constant for YSZ Peak (111), the values for tetragonal ZrO_2 were used [44]. The Al_2O_3 X-ray elastic constants used for the analysis of the TGO considers C14 to be positive [29, 39]. The elastic constants used in the computation of these X-ray elastic constant values were in the units of MPa. The tilt angle (ψ^*) was determined from Equation 3.1. Applying Equation 3.2 along with the Bragg angle specific for each (hkl) crystallographic orientation and the computed tilt angle, the strain free azimuth angle was determined as presented in previous studies [5]. For Equations 3.1 and 3.2, ψ is the tilt angle, S1 and S2/2 are the X-ray elastic constant values, θ_b is the Bragg angle, and η is the strain free azimuth angle. For the sample with CMAS infiltration, the wavelength was $\lambda = 0.1440$ Å and for the sample without CMAS, it was $\lambda = 0.1907$ Å. This variation was because the data collected on both samples were taken at different time periods. Following the approach presented, the strain free azimuth angles calculated for

the samples with CMAS ingression (low density and superdense TBC samples) and the control sample without CMAS ingression (low density TBC sample) are as presented in Table 3.4. The calculation for the strain free azimuth for TGO Peak (300) was performed in a similar manner.

Table 3.3: X-ray Elastic Constant Compliance as determined in the DECcalc Program through use of the material elastic constants [54, 29, 44]

XEC	Al_2O_3 Peak (116)	ZrO_2 Peak (101)
S1	-6.59E-07	-1.71E-06
S2/2	3.32E-06	7.53E-06

Table 3.4: Strain Free Azimuth Angles

Sample	TGO Peak (116)	YSZ Peak (111)
Samples with CMAS	η= 36.995^o	η=41.324^o
Sample without CMAS	η= 36.302^o	η=40.978^o

$$\sin^2(\psi^*) = -2 \cdot (S1/(S2/2)) \tag{3.1}$$

$$\psi = \eta + \theta_b cos(\eta) \tag{3.2}$$

3.3.2 Strain in Thermally Grown Oxide Layer

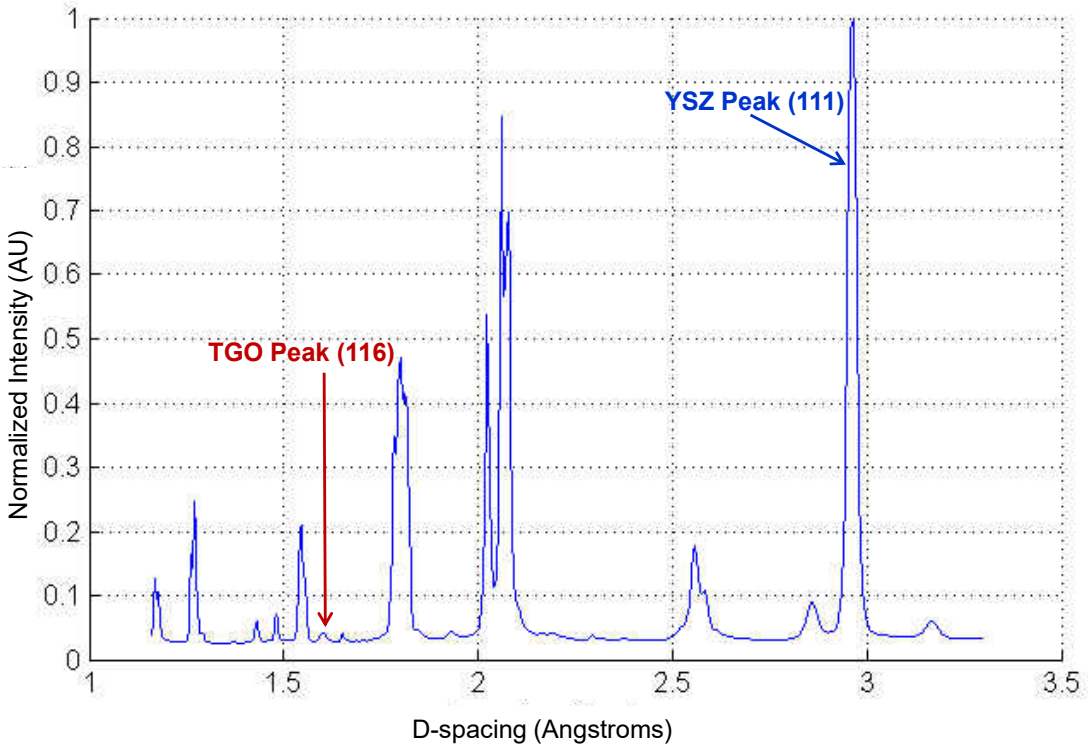

Figure 3.2: Peak Identification Lineout for Low density sample with CMAS ingression

To determine the effect of CMAS on strain within the thermally grown oxide layer, the results presented in this study provide the compressive in-plane strain measurements for TGO peak (116) at a d-spacing of 1.60 Å. Likewise, the strain results presented for

the YSZ layer are for peak (111) at a d-spacing of 2.96 Å. The resulting peak diffraction intensity versus d-spacing for the low density TBC sample with CMAS ingression is shown in Figure 3.2. The intensity for the peaks have been normalized and are the azimuthal average around the 2D diffraction ring.

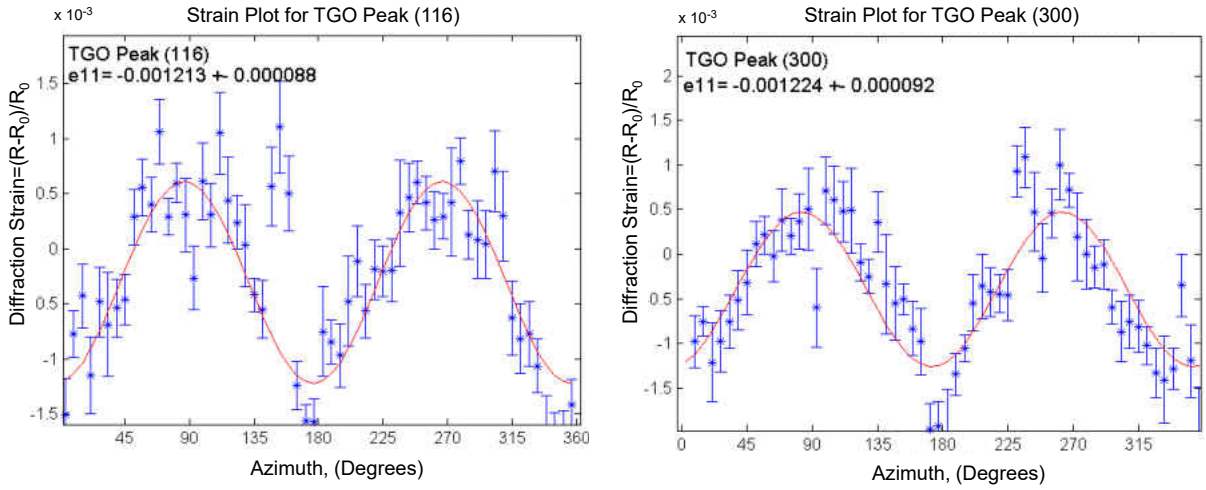

Figure 3.3: Strain Plot of TGO Peaks (116) and (300) for Low density sample with CMAS at room temperature

In order to verify the accuracy of the TGO strain results, a comparison analysis was done between the strain values obtained for TGO Peaks (116) and (300) at room temperature for the sample with CMAS ingression. From Figure 3.3 which plots the resulting diffraction strain versus azimuth, it can be seen that the in-plane (ε_{11}) compressive strain values are very similar, with an in-plane (ε_{11}) strain of -0.001213 and -0.001224 for TGO

peaks (116) and (300) respectively. The strain free azimuth angle calculated for peak (300) of 35.315^o was determined from the same process as presented earlier.

To understand the variation of strain in the TGO under thermal loading conditions, the compressive in-plane strain was plotted during each stage of the 80 minute thermal cycle as shown in Figure 3.4. Both the strain for TGO peak (116) and the temperature are plotted versus the approximate time during the thermal cycle. During ramp up, there is a decrease in the in-plane strain from -0.001213 at room temperature of 26^oC to -0.000404 at 839^oC due to strain relaxation. At high temperatures of around 1121^oC, the in-plane strain value remains approximately constant within the range of -0.000374 to -0.000415. During ramp down, there is a large increase in the compressive strain value in which the in-plane strain value approaches -0.001080 at a temperature of 261^oC. Previous studies have shown this large increase in compressive strain within the TGO layer subjected to thermal loading [7]. The final temperature reading after cycled taken at 64^oC yielded an in-plane strain value of -0.001192 which is approaching the residual strain value noted at room temperature before thermal cycling. The temperatures plotted represent the highest surface temperature recording of the sample by the thermocouples.

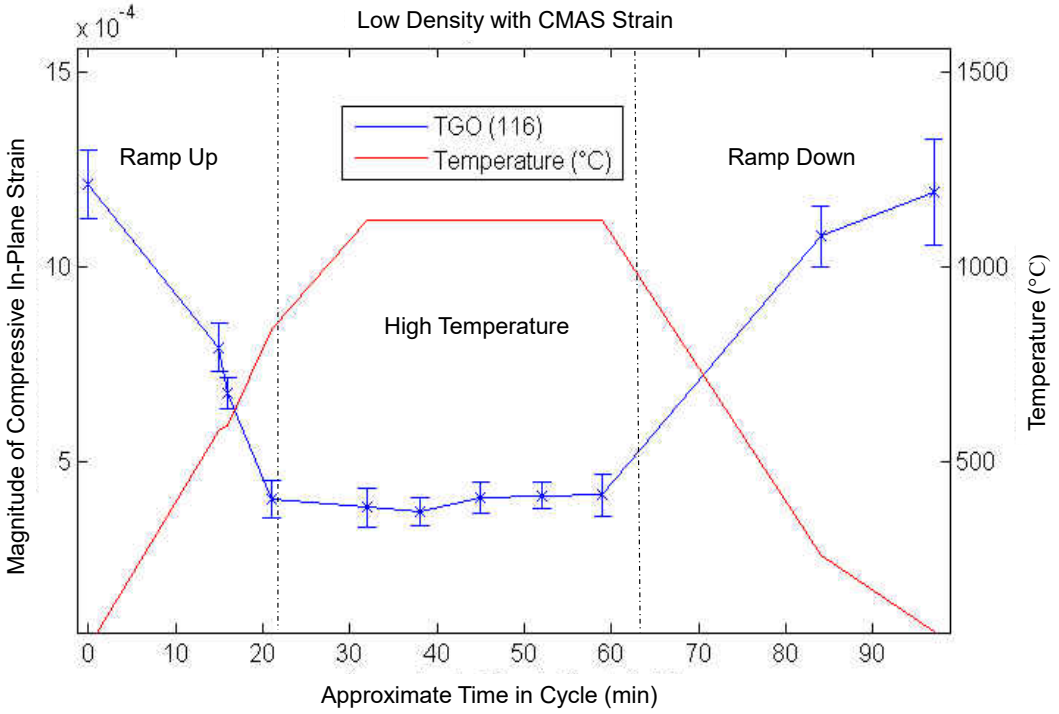

Figure 3.4: Variation of TGO Peak (116) in-plane (ε_{11}) strain and temperature with time during thermal cycle

Table 3.5: Comparison of TGO (116) in-plane (ε_{11}) strain at room temperature for low density samples with and without CMAS infiltration

Sample	Temperature	Compressive In-plane Strain
CMAS sample	26^oC	0.001213
Sample without CMAS	29^oC	0.001131

Through further analysis of the in-plane strain of TGO peak (116) in the control sample without CMAS deposition at room temperature, our results indicate that there is not a significant difference between the strain values in both our sample with CMAS ingression and the sample without CMAS before cycling. These results are presented in Table 3.5. From these results, it is observed that the ingressed CMAS within this sample does not penetrate as far as the thermally grown oxide layer at room temperature to be able to instigate a change in the residual strain of the TGO layer. This correlation of XRD room temperature strain measurements with ingression highlights a promising role in identifying the nature of the ingression and its effect on the mechanical behavior of the layers, which can be applied to various coatings under different ingression materials and conditions.

3.3.3 Strain in YSZ Layer

As previous work has shown, CMAS infiltration plays a role in affecting the thermochemical and thermomechanical properties of the YSZ topcoat. For example, Raman spectroscopy results have shown that the residual stress gradient in regions of CMAS infiltration were tensile and the underlying TBC stress was compressive at ambient temperature [47]. This study was for a DVC TBC sample with deep CMAS penetration of 500 μm. To further examine this behavior, this study has analyzed how CMAS infiltra-

tion alters the YSZ layer's residual strain when subjected to high temperature, for the low density TBC sample with CMAS infiltration. Figure 3.5 presents the in-plane strain results for YSZ peak (111) in the CMAS sample at varying times in the thermal cycle as the X-ray beam passes through the YSZ layer to the TGO interface. Five depth scans were taken on the sample during a 40 minute isothermal hold of $1121^oC \pm 3^oC$. It is important to note that the results presented in Figure 3.5 are not at the exact same depths within the YSZ layer due to thermal expansion variations. It is evident from Figure 3.5 that the in-plane strain for YSZ (111) is tensile as the X-ray beam passes through the YSZ layer. Furthermore, there is a reduction in this tensile strain through the layer. This tensile strain may suggest the presence of CMAS infiltration within the YSZ layer at high temperature, although further metallurgical evaluation will be done in the future to further support this finding. In addition, a transition in the YSZ (111) in-plane strain from tensile to compressive is seen to occur near the interface in all five depth scans where TGO peaks become prominent. This compressive YSZ in-plane strain near the TGO interface would suggest negligible CMAS infiltration near this region. Metallurgical evaluation is suggested as future work to further support this finding. Overall, the YSZ (111) in-plane strain results presented in Figure 3.5, suggest that CMAS infiltration has occured in the YSZ layer, but not near the interface at high temperature.

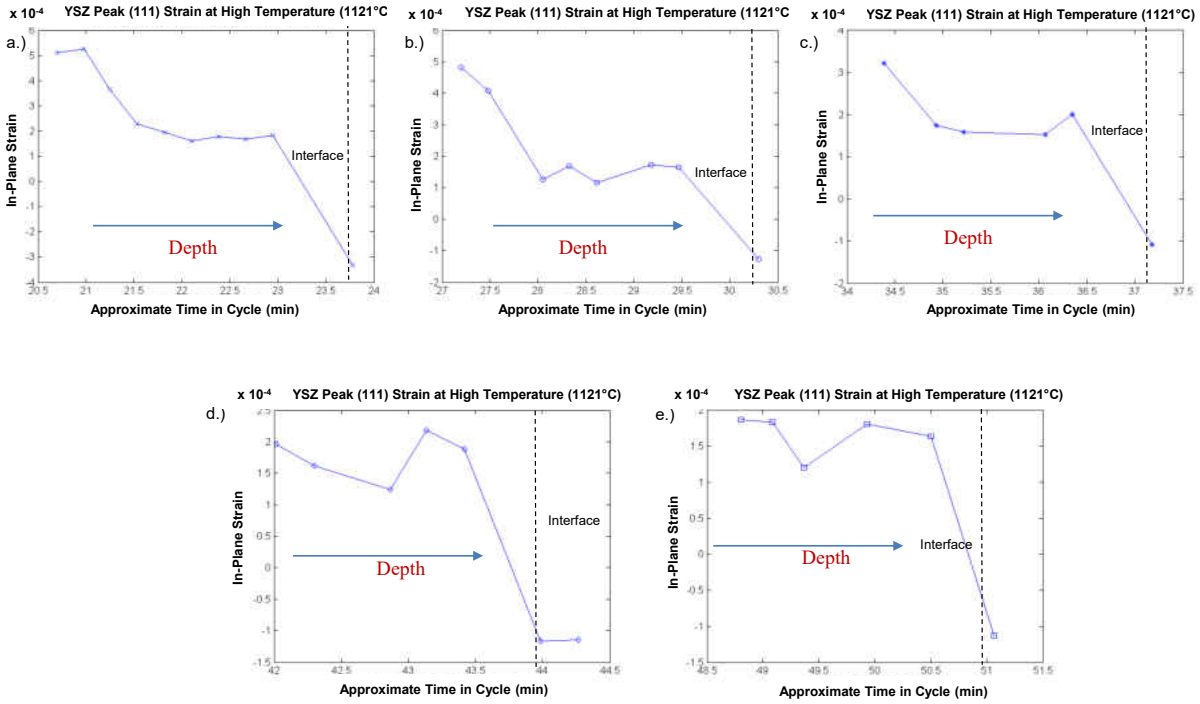

Figure 3.5: Variation of YSZ Peak (111) In-Plane (ε_{11}) Strain at high temperature versus time in the thermal cycle

From Figure 3.6 which is a plot of the resulting diffraction strain versus azimuth for YSZ peak (111) at room temperature, it can be seen that the in-plane strain is compressive with a value of -0.000381. Table 3.6 shows a comparison of YSZ Peak (111) in-plane strain near the TGO interface at room temperature for the low density samples with and without CMAS infiltration. This data was collected before cycling of the samples. As was shown in Table 3.5, there was not a significant difference in the

TGO strain values obtained at room temperature for both samples. This supports the in-plane strain results found for YSZ Peak (111) near the TGO interface, which are also not significantly different.

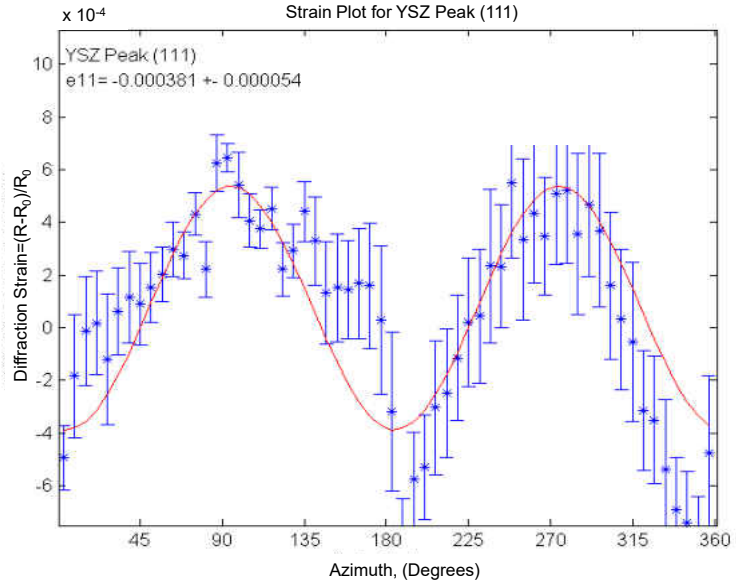

Figure 3.6: Strain Plot of YSZ Peak (111) at room temperature

Table 3.6: Comparison of YSZ (111) in-plane (ε_{11}) strain near TGO Interface at room temperature for low density samples with and without CMAS infiltration

Sample	Temperature	Compressive In-plane Strain
CMAS sample	26^oC	0.000381
Sample without CMAS	29^oC	0.000401

3.4 Superdense TBC Sample with CMAS Results

A previous study by Li et al. has shown that a denser coating has a greater potential to resist CMAS attack than a porous coating [50]. Thus, the motivation of analyzing the strain variation in the thermally grown oxide layer and the YSZ layer near the TGO interface, for a Superdense TBC sample with CMAS, is to characterize this behavior quantitatively. Furthermore, these results can provide strain results for a more dense sample with only 6% porosity. The results presented are based upon the Superdense TBC sample undergoing two thermal cycles.

3.4.1 Strain in YSZ Layer

The strain profile for YSZ Peak (111) near the TGO interface during ramp up and ramp down is shown in Figure 3.7. It can be seen that at room temperature of 30^oC, the in-plane strain within the YSZ layer is highly compressive at a value of -0.001590. During ramp up, from 143^oC to 1036^oC, there is a significant in-plane strain relaxation from -0.001492 to -0.000018. At high temperature of 1124^oC, the in-plane strain becomes slightly tensile with a value of 0.000031. It is important to note this transition in the YSZ Peak (111) in-plane strain from compressive to slightly tensile near the TGO interface could suggest negligible, if any, traces of potential CMAS infiltration near this region.

Finally, during ramp down from 1072^oC to 92^oC, there is a large increase in the in-plane strain compressively from -0.000081 to -0.001502.

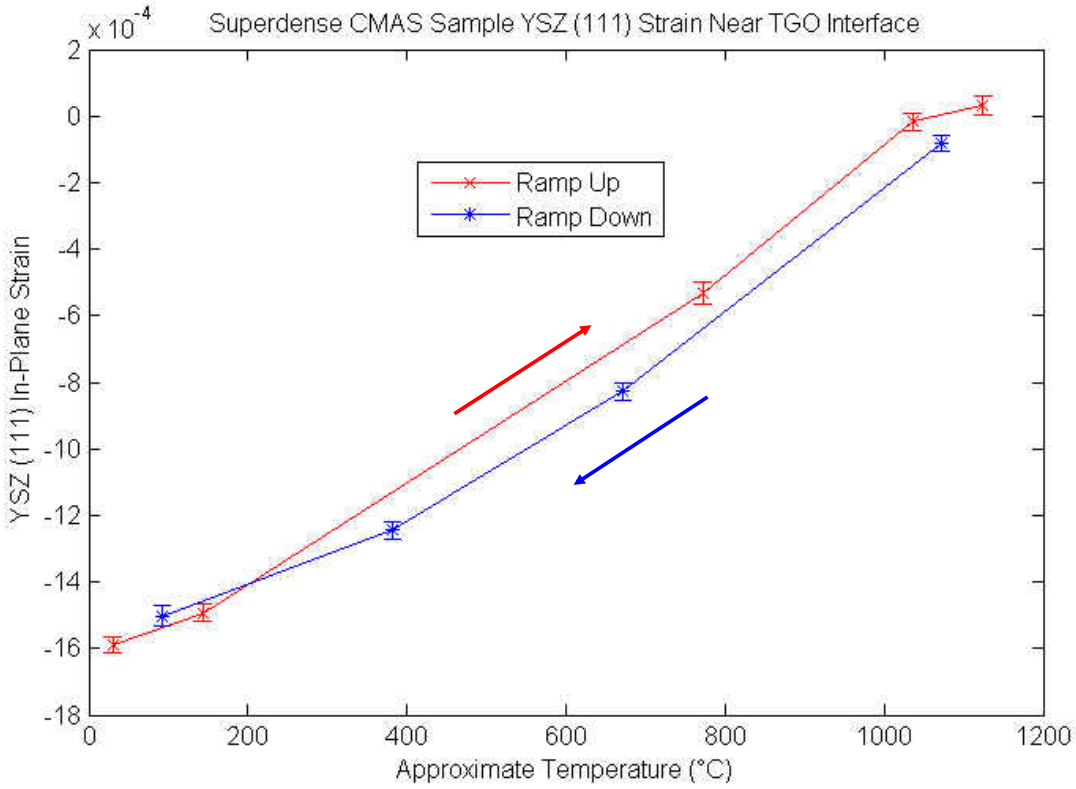

Figure 3.7: YSZ Peak (111) strain near the TGO Interface during ramp up and ramp down in Superdense TBC Sample with CMAS

It can also be observed from Figure 3.7, that there is a lack of significant hysteresis during the thermal cycle from ramp up to ramp down. This would suggest little effect of CMAS infiltration on the in-plane YSZ strain near the TGO interface. As this is

observed for a sample subjected to two 80 minute thermal cycles, future studies will study the effect of various cycles on the presence of hysteresis.

Figure 3.8 shows the resulting diffraction strain versus azimuth fit for YSZ peak (111) near the TGO interface at room temperature. This figure also presents the room temperature in-plane strain for TGO peak (116) and the resulting diffraction strain versus azimuth fit.

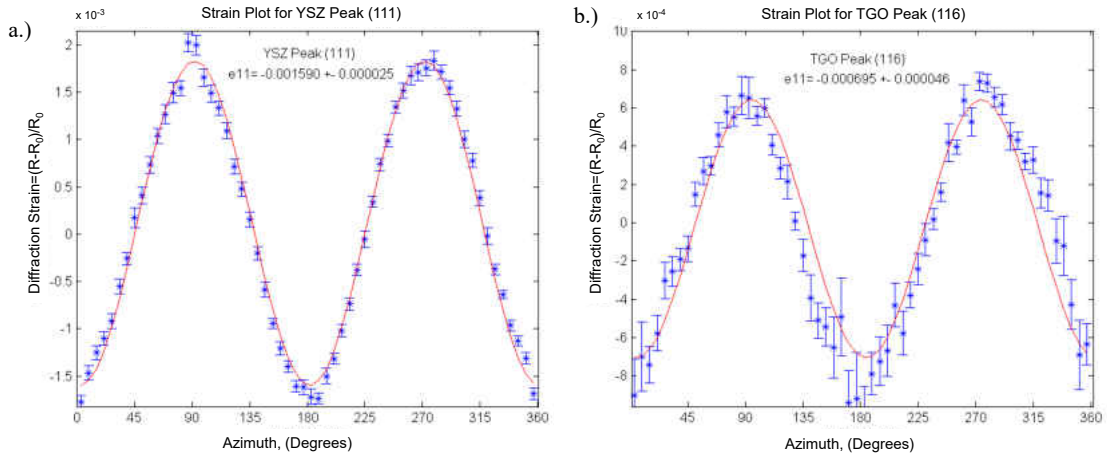

Figure 3.8: Strain Fits at Room Temperature for Superdense TBC Sample with CMAS: a.) YSZ Peak (111) near TGO interface b.) TGO Peak (116)

3.5 Conclusion

In summary, the first part of this study has presented high resolution quantitative strain results for the YSZ and TGO layers of a CMAS plasma sprayed TBC sample of low density deposition under thermal loading conditions. These results show a tensile in-plane strain through the YSZ layer at high temperature. Furthermore, a transition in the YSZ (111) in-plane strain at high temperature from tensile to compressive is observed near the interface. This would suggest CMAS infiltration in the YSZ layer at high temperature, but not near the interface, which will be further supported in the future through metallurgical evaluation. A comparison of TGO in-plane strain values at room temperature between the low density samples with and without CMAS ingression, indicated that there was not a significant effect of CMAS on the strain within the thermally grown oxide layer before cycling. This was further supported by a comparison of the YSZ (111) in-plane strain values near the TGO interface, at room temperature, for low density samples with and without CMAS ingression. It was found that the YSZ (111) in-plane strain near the TGO interface was not significantly different for these samples as well. Future studies with additional cycling are expected to reveal the prolonged effects of cycling on the thermomechanical effects in all layers.

The second part of this study has shown the variation of strain in YSZ peak (111) near the TGO interface, with temperature, for a superdense TBC sample with CMAS infiltration. It has been shown that there is transition in the YSZ Peak (111) in-plane

strain from compressive to slightly tensile near the interface which could suggest negligible, if any traces of CMAS infiltration near this region. Furthermore, there was a lack of significant hysteresis observed, suggesting little change in the YSZ in-plane strain near the TGO interface, as a result of CMAS infiltration.

The technique and methods presented in this chapter have successfully set the stage for future research efforts in ingression studies using X-ray Diffraction under in-situ and high temperature loading conditions.

CHAPTER 4
STRESS MAPPING BY PHOTOLUMINESCENCE SPECTROSCOPY IN TGO UNDULATIONS

4.1 Introduction

The motivation for this study was to characterize variations in TGO critical stresses at a high resolution, that develop within TGO undulations as a result of thermal cycling. Several studies have shown bulk compressive stresses in the TGO that do not accurately reflect the large local variations in stress that occur at the TGO interface [81, 82, 9]. As such, it is important to quantify these large stress variations at a high resolution to ensure improvements in coating durability against common TBC failure mechanisms.

The purpose of this experiment was to nondestructively obtain stress measurements in the peak and trough of a TGO undulation of a DVC 2000 Jets thermal cycled TBC sample at a nanoscale spatial resolution of 200 nm through the use of Photoluminescence spectroscopy. Most importantly, this study is aimed at presenting the variation of local critical stresses in the undulation peak and trough through piezospectroscopy, as a result of the initial 2000 Jet cycles on the sample. The results from this study will allow for a more detailed understanding of how this variation is linked to the initiation of failure mechanisms within a sprayed TBC coating as previous studies have primarily looked at stress mapping in TGO undulations of EB-PVD TBC coatings [81, 82].

4.2 Materials and Methods

4.2.1 Sample Details

High resolution piezospectroscopic measurements were taken at a TGO undulation peak and trough of a dense vertically cracked (DVC) TBC sample that had been previously subjected to 2000 Jets thermal cycles. The importance of having a highly cycled sample for this data collection was to have a fully developed oxide layer, in order to characterize the stress variations. Each Jets thermal cycling process involved heating the YSZ topcoat surface to 1400^oC through an oxygen-propylene burner nozzle for twenty seconds, after which the sample is rotated and cooled by air-blasting for twenty seconds [77]. The DVC TBC sample was also subjected to two 80 minute thermal cycle during preliminary XRD data collection. The DVC TBC coating was applied on a Hast-X substrate and was initially a circular disk with a diameter of 25 mm and a thickness of 5.0 mm. This sample was waterjet cut into a rectangular shape to facilitate data collection on the TGO layer.

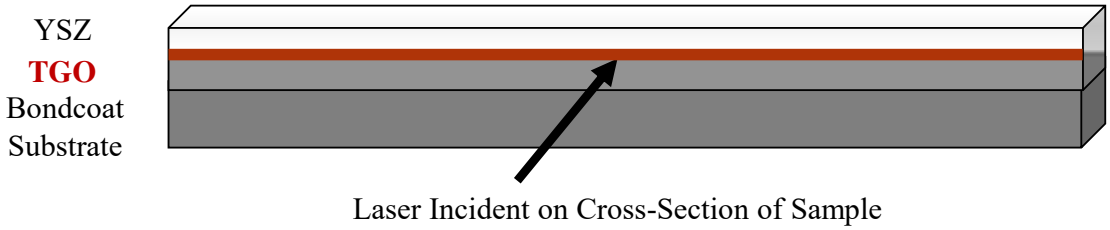

Figure 4.1: Experimental Setup for Photoluminescene Measurements on DVC TBC Sample (Not to Scale)

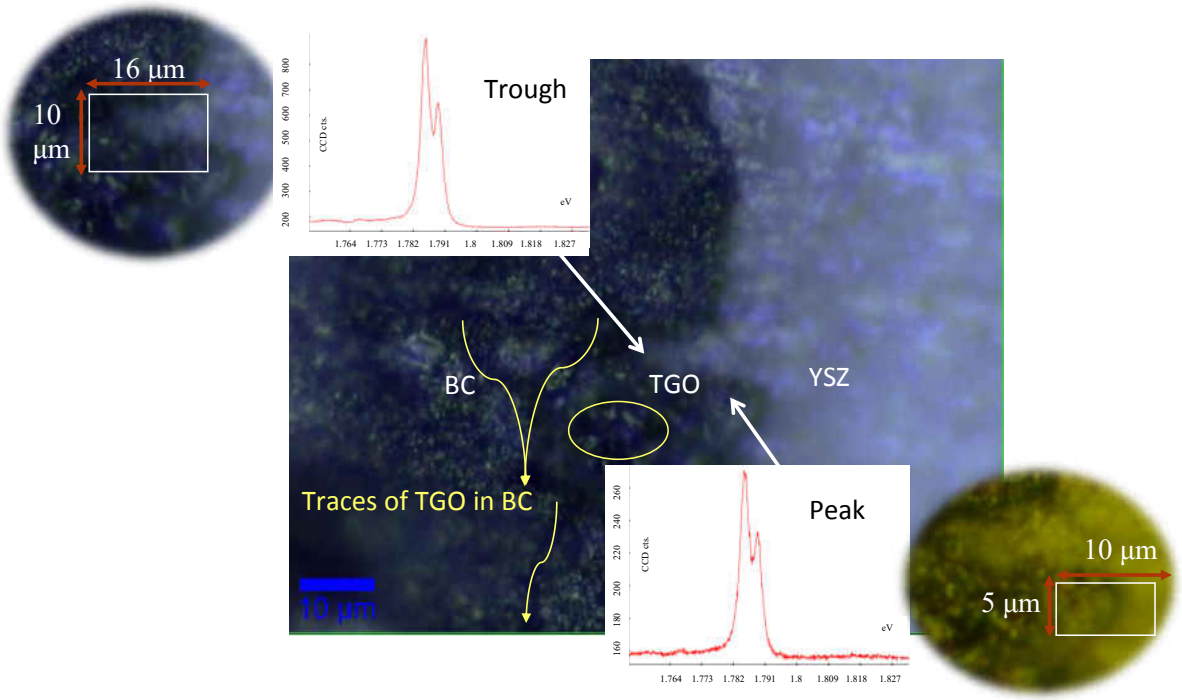

Figure 4.2: TGO Peak and Trough Undulations in DVC 2000 Jets Cycled TBC Sample

4.2.2 High Resolution Photoluminescence Spectroscopy Experimental Details

Photoluminescence Spectroscopy was used to obtain stress maps at room temperature within the peak and trough of a TGO undulation, for a 2000 Jets thermal cycled DVC TBC sample at a resolution of 200 nm in the x and y directions. Photoluminescence measurements were taken on a cross section of the sample at the topcoat and bondcoat interface region in the center of the sample as shown in Figure 4.1.

A 10 μm (x-direction) by 5 μm (y-direction) mapping scan was taken on the peak of the TGO undulation, with data collected on 50 points in the x-direction and 25 points in the y-direction per line. Likewise, a 16 μm (x-direction) by 10 μm (y-direction) mapping scan was taken on the trough of the TGO undulation, with data collected on 80 points in the x-direction and 50 points in the y-direction per line. Mapping in these regions were done row by row. The excitation laser source had a wavelength of 532.24 nm and a power of 5.64 mW. These measurements were taken using an objective lens with a magnification of 50x, using a grating of 1800g/mm, and were collected in the WiTec Project 2.10 software [1]. The R1 and R2 peak positions were initially collected in eV, which were then converted to absolute wavenumber in cm^{-1} for further analysis. Figure 4.2 shows a micrographic image at a scale of 10 μm, of the TGO peak and trough undulation region where these measurements were taken. From the micrographic image, several traces of oxide development within the bondcoat are evident. An example of the

raw R-lines collected in these regions is also displayed in the figure. It is important to note that this figure displays a zoomed in micrograph of both the peak and trough in which the white boxed region defines the approximate mapping area where photoluminescence data was collected.

4.3 Preliminary Results and Discussion

4.3.1 TGO Peak Undulation's Preliminary Residual Stress Measurements in Cycled Sample

The intensity of the alpha-alumina R1 peaks for each of the 1250 data points collected within the TGO peak undulation mapping ($10\mu m$ x $5\mu m$) is shown in a.) of Figure 4.3 at a scale of 1 μm. It is important to note that this figure shows the sum of the CCD counts (calculated from c.) in Figure 4.3) from 14332.47 cm^{-1} to 14418.77 cm^{-1}, which takes into account the CCD count from the R1 peak, whose unstressed position is at 14403 cm^{-1}. Regions of high alumina intensity are seen to be red in the map, while regions of low alumina intensity are seen to be purple. The sum of CCD counts ranges from 2322 to 46720. Figure 4.4 presents the the deconvoluted curve fit of the R-lines obtained for a single point in the first line of the TGO peak mapping, which shows the individual curve fits for R1 and R2 and the fit for both R-lines.

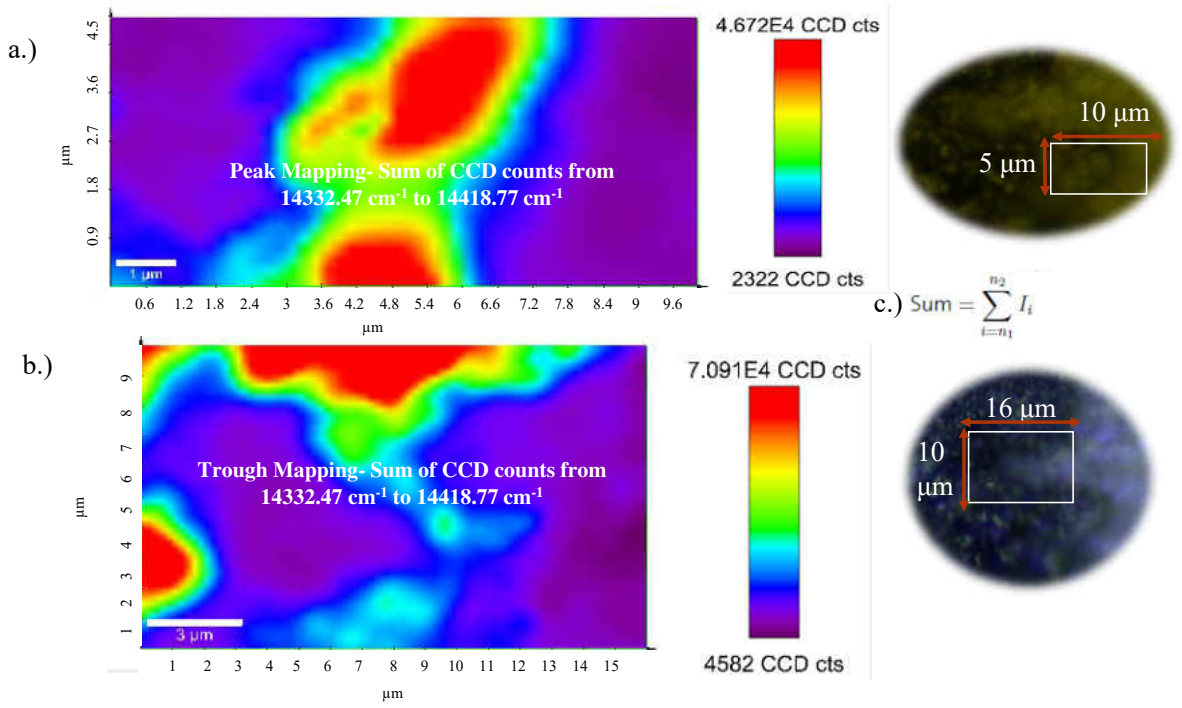

Figure 4.3: Spatial Intensity Maps of R1: a.) Sum of CCD counts for TGO Peak Mapping Scan b.) Sum of CCD counts for TGO Trough Mapping Scan c.) Equation used to sum CCD counts in WiTec software

Figure 4.5 presents preliminary results from the first line of mapping taken in the approximate peak region depicted in Figure 4.2. As shown in Figure 4.2, the mapping scan was taken from the bondcoat to the topcoat, including the TGO layer. The first line of mapping is also from the bondcoat to the topcoat, including the TGO layer. A micrographic image of the peak and approximate location of the single line of data taken is also shown within the figure. The TGO average stress was determined using Equation 2.11 from the R1 peak shift. Figure 4.5 presents both the TGO average stress

and R1 Peak shift versus x-position, which exhibit a similar trend. From the bondcoat to the topcoat, the TGO stress is shown to become less compressive from -0.8592 GPa to -0.4267 GPa, with the largest compressive stress of -0.870 GPa occurring near the bondcoat. These results are expected as seen in several studies of different coating types with average TGO stress in the order of 1 GPa [66], with a large compressive stress occurring near the bondcoat and small compressive stress occurring near the topcoat. Furthermore, an expected non-uniform variation in TGO stress is noted in these plots, which is a result of the large thermal expansion mismatch between the layers of the TBC coating in addition to the development of growth stesses within the TGO layer [81, 82]. However, with this non-uniformity, there is a eminent pattern exhibited in Figure 4.5 which is noted to vary with position. From 0 μm to around 5 μm, when scanning is occurring in the bondcoat/TGO region, TGO stress is seen to exhibit an increasing and decreasing trend. As such, the TGO stress is noted to first become increasingly compressive and then decreasingly compressive. To analyze this variation in more detail, Figure 4.6 shows the micrograph locations of four points taken during this first line scan. Each micrograph image has been marked to approximately indicate the location of each TBC layer (YSZ, TGO and BC). Figure 4.6 further indicates the location of these points on a peak schematic, which gives the approximate location where this single line of data was collected in the TGO peak. It is important to note that this set of data was taken through the peak undulation, not at the edges of the undulation. As shown in the

micrographs of Figure 4.6, points 4 and 10 are near the bondcoat/TGO interface and point 41 is near the TGO/YSZ interface region.

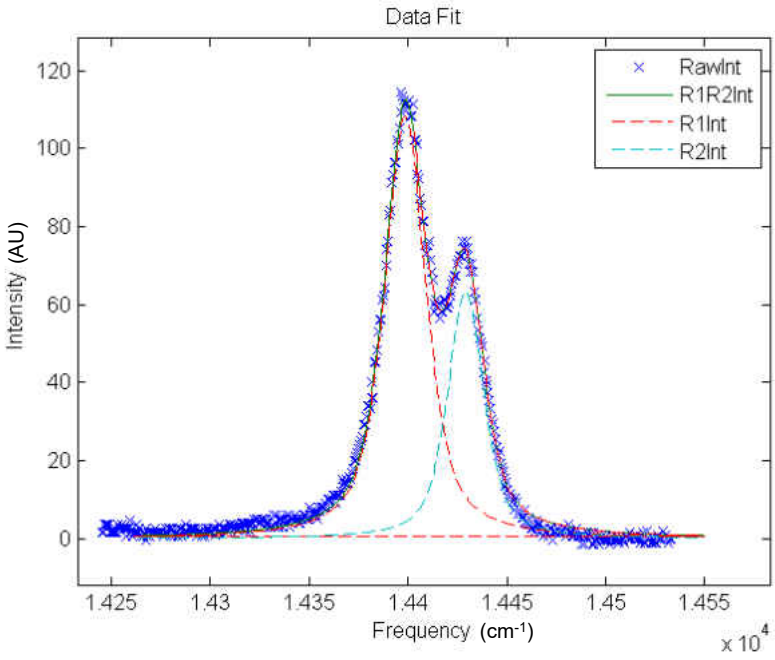

Figure 4.4: Deconvoluted Fit of Single Point from TGO Peak Undulation Mapping

This variation in the TGO stress within the bondcoat and bondcoat/TGO interface region could suggest the presence of Cr_2O_3 in these regions, which has been shown to cause a decrease in the compressive stress and photoluminescence intensity after 100 hours of thermal cycling at 1121^oC [70]. This would imply traces of Cr_2O_3 in locations across this peak scan in which the compressive stress decreases, which is a possibility, because this sample has been previously 2000 Jets cycled. Furthermore, work by Madhwal et al. has shown formation of chromia near the TGO-bondcoat interface during later cycling of a DVC TBC coating [53]. From the micrographic image presented in Figure 4.2, traces

of oxide development in the bondcoat were also evident. This would also suggest the formation of Cr_2O_3, as a result of aluminum depletion within the bondcoat, as well as the possibility that the sample is near failure. However, possibilities of failure initiation will be examined in future work.

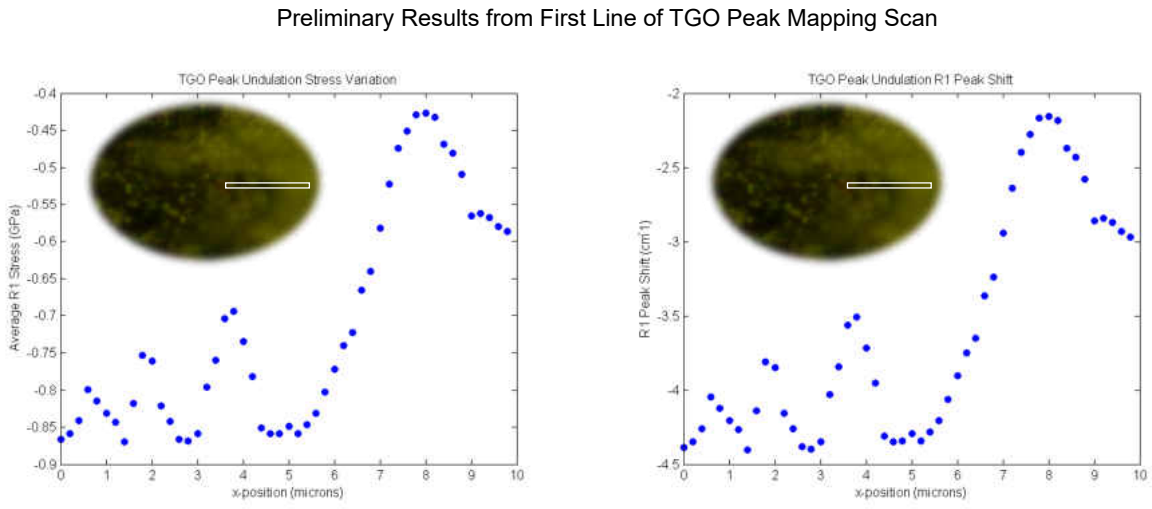

Figure 4.5: Preliminary TGO Stress Results and R1 Peak Shift for First Line of TGO Peak Mapping

Figure 4.3 shows a variation in the R1 CCD intensity counts for the complete peak and trough mapping, which could be a result of traces of Cr_2O_3 concentration. Previous studies have shown that R-line peak intensities are affected by stress variations in the TGO layer as well as Cr concentration [86, 81]. A linear relationship has been shown to exist, between Cr concentration up to 0.5 wt.% in the TGO layer, and R-line peak

intensities [86, 81]. In addition, this variation in R1 intensity could also be associated with variation in surface topology of the probed region.

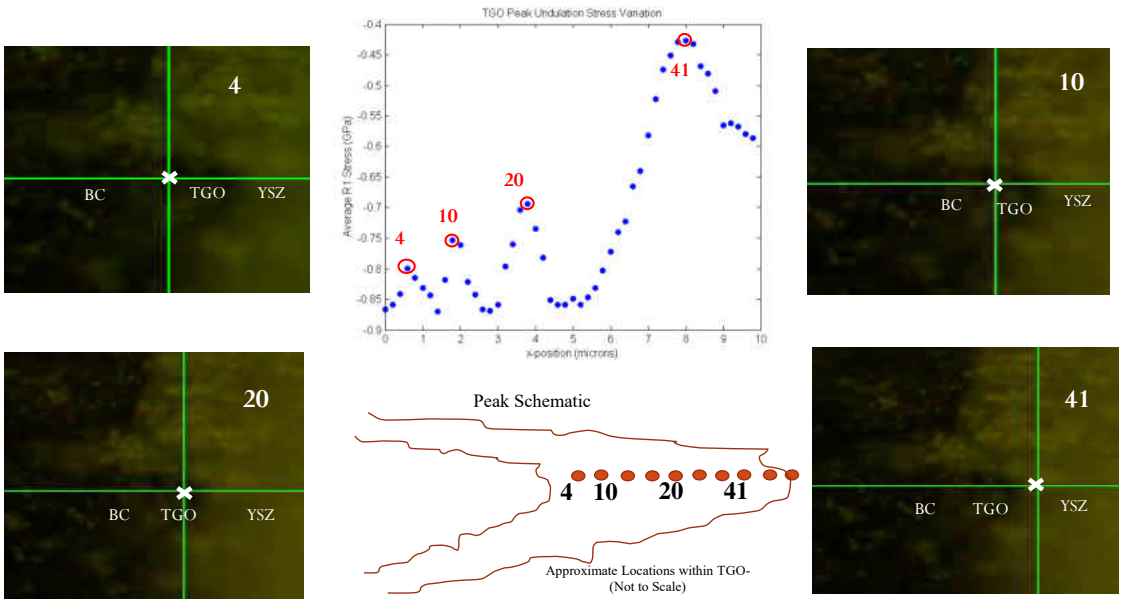

Figure 4.6: Micrographic Locations of Points from First Line of TGO Peak Mapping

Another possibility for this variation in TGO stress is the presence of island-like ceramic oxides that develop within the bondcoat as a result of thermal spray deposition and long exposure at high temperature [83]. These island-like oxides have been shown through simulation to cause a stress relief within the TGO [83], which could also explain the trend that is being seen in Figure 4.5. This possibility can be substantiated by observing the micrograph image of the undulations presented in Figure 4.2, which shows traces of oxide layer development within the bondcoat layer in several locations.

As these preliminary results are only from the first line of mapping taken in the peak region, deconvolution of photoluminescence results from the entire mapping scan in the future will allow for a more thorough understanding of the factors that may be causing this pattern-like variation in the TGO stresses. Therefore, a complete study is needed to further confirm these possibilities for variations, including correlating Atomic Force Microscopy (AFM) imaging with the corresponding PL data.

4.3.2 TGO Trough Undulation's Preliminary Residual Stress Measurements in Cycled Sample

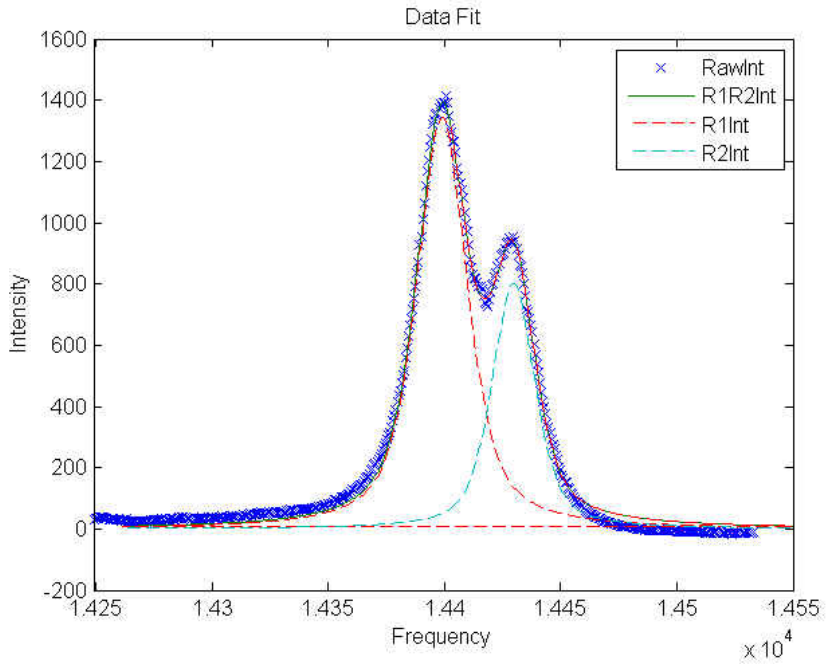

Figure 4.7: Deconvoluted Fit of Single Point from TGO Trough Undulation Mapping

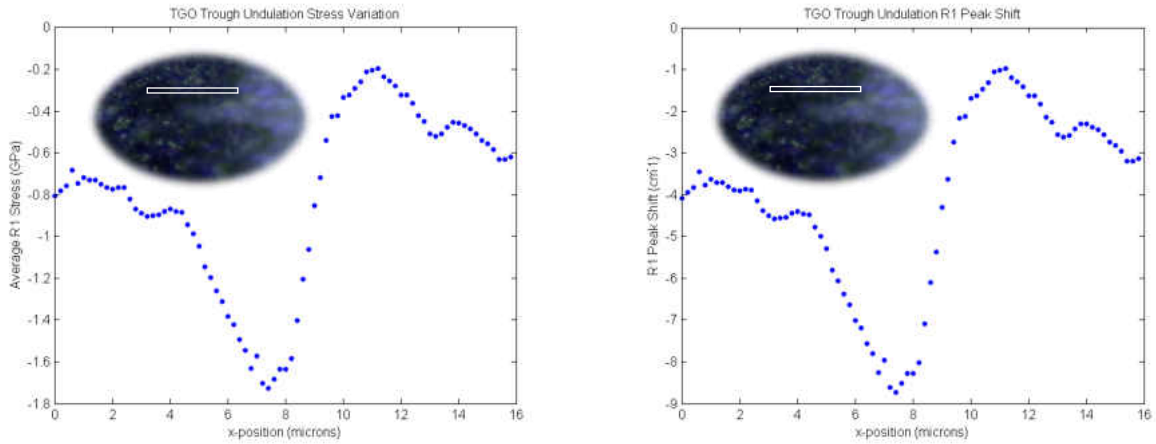

Figure 4.8: Preliminary TGO Stress Results and R1 Peak Shift for First Line of TGO Trough Mapping

The intensity of the alpha-alumina R1 peaks for each of the 4000 data points collected within the TGO trough undulation mapping ($16\mu m$ x $10\mu m$) is shown in b.) of Figure 4.3 at a scale of 3 μm. It is important to note that this figure also shows the sum of the CCD counts from 14332.47 cm^{-1} to 14418.77 cm^{-1}, which takes into account the CCD count from R1 peak, whose unstressed position is at 14403 cm^{-1}. Regions of high alumina intensity are seen to occur towards the top and lower left regions of the map. From the micrographic image, this occurs at the TGO interface region. Further evident from the plot, are low intensities of alumina within the YSZ region. This suggests slight traces of TGO development within this region. The sum of CCD counts is seen to range from

4582 to 70910 and was calculated from c.) in Figure 4.3. Deconvoluted fit of a single point in the first line of the TGO trough mapping is shown in Figure 4.7.

Figure 4.8 presents preliminary results from the first line of mapping taken in the approximate trough region depicted in Figure 4.2. As shown in Figure 4.2, the mapping scan was taken from the bondcoat into to the topcoat, including the TGO layer. The first line of mapping in the trough was primarily in the bondcoat region near the TGO interface, which extends slightly into the YSZ layer, as shown in the micrographic image in this figure. The TGO average stress was determined using Equation 2.11 from the R1 peak shift. Figure 4.8 presents both the TGO average stress and R1 Peak shift versus x-position, which also exhibits a similar trend. It can be seen that the TGO stress first becomes more compressive, from -0.8056 GPa to -1.7254 GPa in the region from 0 μm to 7.4 μm, and then becomes less compressive, from -1.7254 GPa to -0.1944 GPa in the region from 7.4 μm to 11.2 μm. Finally, the stress is seen to become more compressive from -0.1944 GPa to -0.6194 GPa, in the region from 11.2 μm to 15.8 μm. The expected non-uniform variation in TGO stress is noted in these plots as well the large variation shown in TGO stress values [82, 81]. Similar to the first line mapping of the peak region, there is the presence of a similar trend regarding the variation of stress in this first line mapping of the trough region. However, it is important to note that unlike the results presented for the peak region, there is a much larger variation in the maximum and minimum stress values found in the trough region.

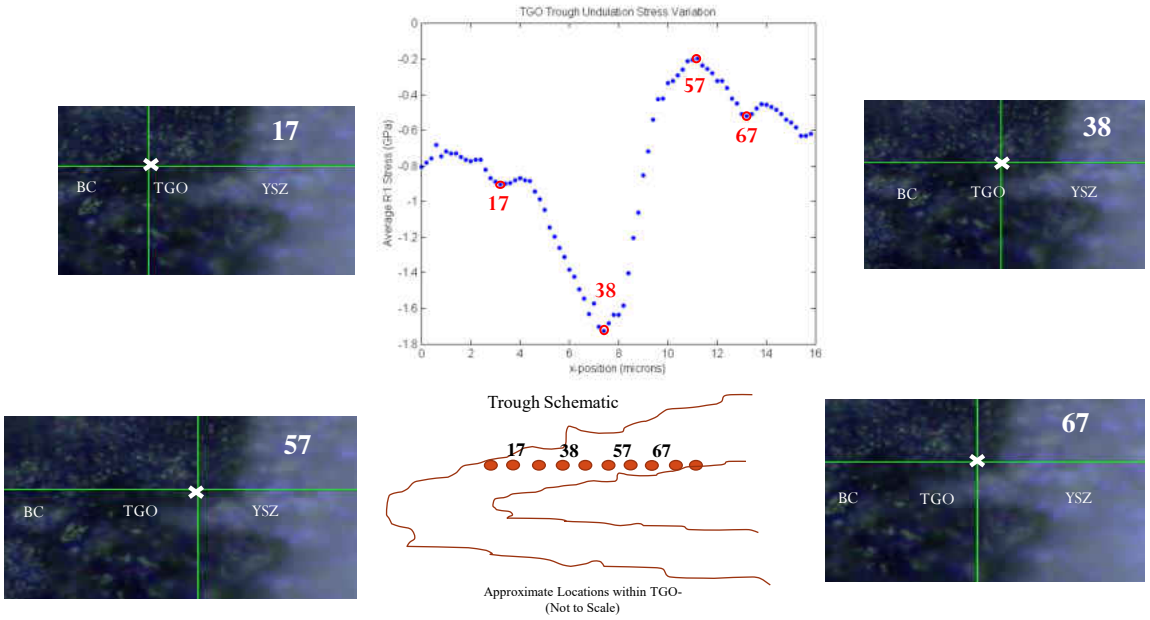

Figure 4.9: Micrographic Locations of Points from First Line of TGO Trough Mapping

Figure 4.9 shows the micrograph locations of four points taken during this first line scan in the trough region. Each micrograph image has been marked to approximately indicate the location of each TBC layer (YSZ, TGO and BC). Figure 4.9 further indicates the location of these points on a trough schematic, which gives the approximate location where this single line of data was collected in the TGO trough. It is important to note that this single line data was taken near the edge of the trough undulation. Furthermore, points 17 and 38 were found to be located in regions with high alumina intensity whereas points 57 and 67 were located in regions of low alumina intensity. This is a viable possibility for the large variation in TGO stress shown in Figure 4.8. From the micrograph images of the location of points 17, 38, 57 and 67, it is evident that there is a change in the undulation geometry. It has been previously suggested that TGO stress concentrates

at points of greater curvature [83]. This study by Wang et al. has further suggested that since the TGO undulation is becoming more steep, there tends to be a stress concentration at a location with higher curvature [83]. Therefore, an additional possibility for this variation in TGO stress in the trough region can be attributed to variation in the undulation/rumpling geometry as shown in other studies [72]. Other possibilities for this variation could be the presence of other phases within this bondcoat/TGO region including traces of Cr_2O_3 or island-like ceramic oxides as mentioned with the single line peak results.

As these preliminary results are only from the first line of mapping taken in the trough region, deconvolution of photoluminescence results from the entire mapping scan, correlated with AFM imaging of the locations in the future, will allow for a more thorough understanding of the factors that may be causing this variation in the TGO stresses. Similar to the single line peak analysis, a more complete study is needed to further confirm these possibilities for variations in the trough region.

4.4 Conclusion

This study has presented preliminary high resolution TGO stress results from the peak and trough regions of a Jets cycled DVC TBC sample at a resolution of 200 nm through photoluminescence spectroscopy. Findings from the first line analysis in the peak and

trough regions have shown a non-uniform TGO stress distribution, with the stress becoming less compressive from the bondcoat to the topcoat.

From the first line analysis of TGO stress in the peak region, a variation is seen to occur during scanning from the bondcoat to the topcoat, including the TGO layer. As these are preliminary findings, analysis of the complete mapping scan will yield more complete results. This variation is most prominent in the bondcoat and bondcoat/TGO interface region. Potential causes for this variation could be the presence of Cr_2O_3 which has been shown to cause a decrease in the compressive stress [70], or the presence of island-like ceramic oxides within the bondcoat that have been shown through simulation to cause a stress relief within the TGO [83]. The large variation in TGO stress from -0.8592 GPa to -0.4267 GPa can be attributed to scanning from the TGO interface into the YSZ layer near the TGO interface.

The first line analysis of the trough region was primarily in the bondcoat region near the TGO interface, which extended slightly into the YSZ layer. From the first line analysis of TGO stress in the trough region, a large variation in TGO stress is noted from -1.7254 GPa to -0.1944 GPa. A trend in the TGO stress variation was also found in the first line analysis of the trough region. Possible causes for this variation could be the change in undulation geometry, which would suggest TGO stress concentration at points of greater curvature [83], or variation in alumina concentration. Other possibilities for this variation could be the presence of other phases within this bondcoat/TGO region including traces of Cr_2O_3 or island-like ceramic oxides as mentioned with the single line

peak results. It is important to note that these findings are preliminary and complete results from the entire mapping scans taken in the peak and trough are necessary to determine the factors that are causing these variations in the TGO stress.

CHAPTER 5
CONCLUSION

5.1 Effect of CMAS on Strain in Layers of the TBC

The effect of CMAS on the in-plane strain in the YSZ topcoat and TGO layers of sprayed TBCs, under thermal cycling conditions, has been presented in this study. This has been achieved through in-situ synchrotron X-ray diffraction measurements.

This study has found that for a low density plasma sprayed CMAS sample, a transition in the YSZ in-plane strain occurs from tensile to compressive near the TGO interface at high temperature. Furthermore, through the YSZ layer, a tensile in-plane strain is observed at high temperature. Quanitative strain measurements in the TGO layer of the low density with CMAS sample were presented for the entire thermal cycle. Strain relaxation was noted to occur during ramp up and a large increase in compressive strain was found during ramp down to room temperature.

A comparison of the TGO in-plane strain values at room temperature for low density samples with and without CMAS infiltration indicated that there was not a significant difference in the strain values within the thermally grown oxide layer before cycling. This was further supported by comparison of the YSZ (111) in-plane strain values near the TGO interface for the same samples, which were also found to not be significantly different.

This study has also shown variation of strain in YSZ peak (111) near the interface during the entire thermal cycle, for a superdense TBC sample with CMAS. At high temperature, a slightly tensile YSZ strain is seen to occur near the interface, suggesting negligible, if any, infiltration of CMAS in this region. Furthermore, the presence of minimal hysteresis indicates that there is little effect of CMAS infiltration on YSZ in-plane strain near the TGO interface.

Overall, the in-situ XRD technique used in this study to capture strain measurements in CMAS ingressed samples under thermal loading conditions, can be used towards future studies of ingression from CMAS, volcanic ash and fuel impurities. This technique has allowed for a more thorough understanding of CMAS ingression on the thermomechanical effects seen within TBC coatings as a result of CMAS ingression. The experimental findings from this study can be used towards finite element simulations of strain variation as a result of CMAS infiltration and furthermore towards improvements in TBC coating durability to reduce errosion-based failures of these coatings.

5.2 Stress Mapping by High Resolution Photoluminescence Spectroscopy in TGO Undulations

High resolution preliminary stress results, on the order of 200 nm, have been presented in the peak and trough of a TGO undulation within a Jets cycled DVC TBC sample in this study. This has been achieved through photoluminescence spectroscopy measurements

at room temperature. First line analysis of mapping scans within the peak and trough regions have shown a non-uniform TGO stress distribution versus position. Similarly, the R1 peak shift versus position have shown a non-uniform variation. The largest variation in TGO stress in the first line mapping of the peak region occurred from -0.8592 GPa to -0.4267 GPa. This variation is suggested to be a result of scanning from the TGO interface into the YSZ layer near the TGO interface. For first line mapping of the trough region, a large variation in stress is also noted from -1.7254 GPa to -0.1944 GPa.

Both sets of preliminary results have exhibited a trend in TGO stress variation. From the first line analysis of TGO stress in the peak region, an increasing and decreasing variation is seen to occur during scanning from the bondcoat to the topcoat, including the TGO layer. This variation is most prominent in the bondcoat region with TGO development and bondcoat/TGO interface region. Potential causes for this variation could be the presence of Cr_2O_3 which has been shown to cause a decrease in the compressive stress [70], or the presence of island-like ceramic oxides within the bondcoat that have been shown through simulation to cause a stress relief within the TGO [83].

The trend in the first line mapping of the trough region may be caused by change in undulation geometry, which would suggest TGO stress concentration at points of greater curvature [83] or variation in alumina concentration. Other possibilities for this variation could be the presence of other phases within this bondcoat/TGO region including traces of Cr_2O_3 or island-like ceramic oxides as mentioned with the first line peak results.

These results are preliminary findings and as such, a few possibilities have been suggested in this study, to explain this trend-like behavior. However, future analysis of the entire peak and trough mapping region will allow for a more thorough understanding of the factors that are causing this trend-like variation in the TGO stress within these regions.

The preliminary results from this study have shown the need for analyzing the mechanics of layered materials at a high spatial resolution. Most importantly, these findings have shown a significant variation in TGO stresses at a high spatial resolution, which can be used to understand the evolution of these local, critical stresses under operating conditions that lead to the initiation of failure mechanisms within the TBC coating. This study has also shown that the assumptions of simple 2D flat layers needs to be accompanied with the geometric features of the TGO undulations, which give rise to these significant stress variations, and ultimately have an impact on the initiation of damage in TBC coatings. Future analysis of these local stresses can lead to improvements in the durability of these coatings.

5.3 Future Work

The current study presented in-situ synchrotron XRD in-plane strain results under thermal loading conditions, in the YSZ and TGO layers of sprayed TBC coatings with CMAS infiltration. This study can be improved by characterizing the strain in EB-PVD TBC

coatings with CMAS infiltration under thermal loading conditions. Furthermore, a comparison analysis between the strain tolerance of both types of coatings under CMAS attack would provide substantial information on how to improve the durability of these coatings.

This study has also presented preliminary R1 peak shift and average stress results at a resolution of 200 nm from the top line of a TGO peak and trough undulation mapping, in a 2000 Jets Cycled DVC TBC Sample. Future work will entail deconvolution of the photoluminescence data obtained for this entire mapping scan in the TGO peak and trough undulation.

In addition, high resolution stress measurements will be taken in the TGO undulations using NSOM (Near-field Scanning Optical Microscopy)-PL (Photo-Luminescence) spectroscopy, which has the potential to provide spatial resolution of 100 nm or less [79]. A comparison of TGO stress results with varying spatial resolution will be considered. These results can also be compared with X-ray TGO diffraction data collected on the sample at room temperature and under thermal cycling conditions. Additional studies can use finite element simulation to characterize the stress variation in these TGO undulations to compare with experimentally collected data.

LIST OF REFERENCES

[1] WITec GmbH. WITec Project Data Evaluation Software 2.10.

[2] Aluminum Oxide: JCPDS No. 00-042-1468. Technical report, Joint Committee on Powder Diffraction Standards of the International Centre for Diffraction Data (ICDD), 2010.

[3] Zirconium Yttrium Oxide: JCPDS No. 01-070-4430. Technical report, Joint Committee on Powder Diffraction Standards of the International Centre for Diffraction Data (ICDD), 2010.

[4] Zirconium Oxide: JCPDS No. 00-017-0923. Technical report, Joint Committee on Powder Diffraction Standards of the International Centre for Diffraction Data (ICDD), 2012.

[5] J. Almer, U. Lienert, R. L. Peng, C. Schlauer, and M. Oden. Strain and texture analysis of coatings using high energy x-rays. *Journal of Applied Physics*, 94:697–702, 2003.

[6] J. Almer and S. Stock. Internal strains and stresses measured in cortical bone via high-energy x-ray diffraction. *Journal of Structural Biology*, 152:14–27, 2005.

[7] J. Almer, G. Swift, J. Nychka, E. Ustundag, and D. R. Clarke. In situ synchrotron measurements of oxide growth strains. *Materials Science Forum*, 490-491:287–293, 2005.

[8] P. F. Batcho. Interpretation of gas turbine response due to dust ingestion. Technical report, Defense Nuclear Agency, 1986.

[9] H. Bhatnagar, S. Ghosh, and M. E. Walter. Parametric studies of failure mechanisms in elastic EBPVD thermal barrier coatings using FEM. *International Journal of Solids and Structures*, 43:4384–4406, 2006.

[10] H. Bhatnagar, S. Ghosh, and M. E. Walter. A parametric study of damage initiation and propagation in EB-PVD thermal barrier coatings. *Mechanics of Materials*, 42(1):96–107, 2010.

[11] M. P. Borom, C. A. Johnson, and L. A. Peluso. Role of environmental deposits and operating surface temperature in spallation of air plasma sprayed TBC. *Surface and Coatings Technology*, 86-87:116–126, 1996.

[12] E. Brinksmeier and H. Siemer. Calculation of x-ray elastic constants of aluminum oxide ceramics. In *Proceedings of the International Conference on Residual Stresses*, pages 335–340, 1989.

[13] W. Chen, X. Wu, B. Marple, and P. Patnaik. The growth and influence of thermally grown oxide in a thermal barrier coating. *Surface Coatings and Technology*, 201:1074–1079, 2006.

[14] X. Chen. CMAS delamination mechanisms in EB-PVD thermal barrier coatings. *Surface & Coatings Technology*, 200:3418–3427, 2006.

[15] R. J. Christensen, D. M. Lipkin, and D. R. Clarke. Nondestructive evaluation of the oxidation stresses through thermal barrier coatings using Cr^{3+} piezospectroscopy. *Applied Physics Letters*, 69:3754–3756, 1996.

[16] D. R. Clarke, R. J. Christensen, and V. Tolpygo. Evolution of oxidation stresses in zirconia thermal barrier coated superalloy leading to spalling failure. *Surface Coatings and Technology*, 94-95:89–93, 1997.

[17] D. R. Clarke and C. G. Levi. Materials design for the next generation thermal barrier coatings. *Annual Review of Materials Research*, 33:383–417, 2003.

[18] R. Diaz, M. Jansz, M. Mossaddad, S. Raghavan, J. Okasinski, J. Almer, H. Pelaez-Perez, and P. Imbrie. Role of mechanical loads in inducing in-cycle tensile stresses in thermally grown oxide. *Applied Physics Letters*, 100:111906, 2012.

[19] R. O. Diaz. In-situ stress measurements of EB-PVD thermal barrier coatings using synchrotron x-ray diffraction under thermo-mechanical loading. Master's thesis, University of Central Florida, 2010.

[20] J. M. Drexler, A. Aygun, D. Li, R. Vaben, T. Steinke, and N. P. Padture. Thermal-gradient testing of thermal barrier coatings under simultaneous attack by molten glassy deposits and its mitigation. *Surface and Coatings Technology*, 204:2683–2688, 2010.

[21] M. G. Dunn, A. J. Baren, and J. Miatech. Operation of gas turbine engines in volcanic ash. *ASME*, 118:724–731, 1996.

[22] M. G. Dunn, C. Padova, J. E. Moller, and R. M. Adams. Performance deterioration of turbofan and a turbojet engine upon exposure to a dust environment. *ASME*, 109:336–343, 1987.

[23] A. G. Evans, M. Y. He., and J. W. Hutchinson. Mechanics-based scaling laws for the durability of thermal barrier coatings. *Progress in Materials Science*, 46:249–271, 2001.

[24] A. G. Evans, D. R. Mumm, J. W. Hutchinson, G. H. Meier, and F. S. Pettit. Mechanisms controlling the durability of thermal barrier coatings. *Progress in Materials Science*, 46:505–553, 2001.

[25] H. E. Evans. Oxidation failure of TBC systems: An assessment of mechanisms. *Surface and Coatings Technology*, 206(7):1512–1521, 2011.

[26] L. France, N.Ouillon, G.Chazot, J.Kornprobst, and P.Boivin. CMAS 3D, a new program to visualize and project major elements compositions in the CMAS system. *Computers & Geosciences*, 35:1304–1310, 2009.

[27] H. F. Garces, B. S. Senturk, and N. P. Padture. In-situ Raman spectroscopy studies of high-temperature degradation of thermal barrier coatings by molten silicate deposits. *Scripta Materialia*, 76:29–32, 2014.

[28] M. Gell, S. Sridharan, and M. Wen. Photoluminescence piezospectroscopy: A multipurpose quality control and NDI technique for thermal barrier coatings. *International Journal of Applied Ceramics Technology*, 1:316–329, 2004.

[29] J. Gladden, J. H. So, J. Maynard, P. Saxe, and Y. L. Page. Reconciliation of ab initio theory and experimental elastic properties of Al_2O_3. *Applied Physics Letters*, 85, No. 3:392–394, 2004.

[30] L. Grabner. Spectroscopic technique for the measurement of residual stress in sintered Al_2O_3. *Journal of Applied Physics*, 49(5):580–583, 1978.

[31] K. M. Grant, S. Krämer, J. P. Löfvander, and C. G. Levi. CMAS degradation of environmental barrier coatings. *Surface & Coatings Technology*, 202:653–657, 2007.

[32] A. P. Hammersley. European Synchrotron Research Facility (ESRF), Internal Report. ESRF98HA01T, FIT2D V9.129 Reference Manual V3.1. Technical report, ESRF, Grenoble, France, 1998.

[33] A. P. Hammersley, S. O. Svensson, and A. Thompson. Calibration and correction of spatial distortions in 2D detector systems. *Nucl. Instr. Meth.*, A346:312–321, 1994.

[34] B. J. Harder, J. J. Ramirez-Rico, J. D. Almer, K. N. Lee, and K. T. Faber. Chemical and Mechanical Consequences of Environmental Barrier Coating Exposure to Calcium-Magnesium-Aluminosilicate. *Journal of American Ceramic Society*, 94:178–185, 2011.

[35] V. Hauk. *Structural and Residual Stress Analysis by Nondestructive Methods*. Elsevier Science, 1997.

[36] B. He. Introduction to two dimensional xray diffraction. *Powder Diffraction*, 18(2):71–85, June 2003.

[37] J. He and D. R. Clarke. Determination of the piezospectroscopic coefficients for chromium doped sapphire. *Journal of American Ceramic Society*, 78(5):1347–1353, 1995.

[38] R. Hillery, B. Pilsner, R. McKnight, T. Cook, and M. Hartle. Thermal barrier coating life prediction model development. Technical report, NASA, 1988.

[39] D. B. Hovis, A. Reddy, and A. H. Heuer. X-ray elastic constants for $\alpha - Al_2O_3$. *Applied Physics Letters*, 88:131910, 2006.

[40] A. M. Karlsson and A. G. Evans. A numerical model for the cyclic instability of thermally grown oxides in thermal barrier systems. *Acta Materialia*, Volume 49 Issue 10:1793–1804, 2001.

[41] A. M. Karlsson, J. W. Hutchinson, and A. G. Evans. A fundamental model of cyclic instabilities in thermal barrier systems. *Journal of the Mechanics and Physics of Solids*, 50:1565–1589, 2002.

[42] A. M. Karlsson, T. Xu, and A. G. Evans. The effect of the thermal barrier coating on the displacement instability in thermal barrier systems. *Acta Materialia*, 50(5):1211 – 1218, 2002.

[43] J. Kim, M. Dunn, A. Baran, D. Wade, and E. Tremba. Deposition of volcanic materials in the hot sections of two gas turbine engines. *Journal of Engineering for Gas Turbines and Power*, 115, 1993.

[44] E. H. Kisi and C. J. Howard. Elastic constants of tetragonal zirconia measured by a new powder diffraction technique. *Journal of the American Ceramic Society*, 81 No.6:1682–1684, 1998.

[45] K. Knipe, A. Manero, S. F. Siddiqui, C. Meid, J. Wischek, J. Okasinski, J. Almer, A. M. Karlsson, M. Bartsch, and S. Raghavan. Strain response of thermal barrier coatings captured under extreme engine environments through synchrotron x-ray diffraction. *Nature Communications*, Letter Manuscript Accepted for Publication, 2014.

[46] N. Koch and H. Wern. Selfconsistent determination of the x-ray elastic constants of polycrystalline materials for arbitrary crystal symmetry. *JCPDS- International Centre for Diffraction Data 2002, Advances in X-Ray Analysis*, 45:200–205, 2002.

[47] S. Krämer, S. Faulhaber, M. Chambers, D. R. Clarke, C. G. Levi, J. W. Hutchinson, and A. G. Evans. Mechanisms of cracking and delamination within thick thermal barrier systems in aero-engines subject to calcium-magnesium-alumino-silicate (CMAS) penetration. *Materials Science and Engineering: A*, 490(1-2):26–35, 2008.

[48] S. Krämer, J. Yang, C. A. Johnson, and C. G. Levi. Thermochemical interaction of thermal barrier coatings with molten CMAS. *Journal of the American Ceramic Society*, 89:3167–3175, 2006.

[49] C. G. Levi, J. W. Hutchinson, Marie-Hélène, Vidal-Sétif, and C. A. Johnson. Environmental degradation of thermal-barrier coatings by molten deposits. *MRS Bulletin*, 37, 2012.

[50] L. Li, N. Hitchman, and J. Knapp. Failure of thermal barrier coatings subjected to CMAS attack. *Journal of Thermal Spray Technology*, 19:148–155, 2010.

[51] D. M. Lipkin and D. R. Clarke. Sample-probe interactions in spectroscopy: Sampling microscopic property gradients. *Journal of Applied Physics*, 77:1855–1863, 1995.

[52] Q. Ma and D. R. Clarke. Stress measurement in single-crystal and polycrystalline ceramics using their optical fluorescence. *Journal of the American Ceramic Society*, 76(6):1433–1440, 1993.

[53] M. Madhwal, E. H. Jordan, and M. Gell. Failure mechanisms of dense vertically-cracked thermal barrier coatings. *Materials Science and Engineering*, A 384:151–161, 2004.

[54] T. Manns and B. Scholtes. A software for the calculation of diffraction elastic constants from single crystal coefficients. *Journal of Heat Treatment and Materials*, 65 No. 2:75–84, 2010.

[55] C. Mercer, S. Faulhaber, A. G. Evans, and R. Darolia. A delamination mechanism for thermal barrier coatings subject to CMAS infiltration. *Acta Materialia*, 53:1029–1039, 2004.

[56] P. Mohan, T. Patterson, B. Yao, and Y. Sohn. Degradation of thermal barrier coatings by fuel impurities and CMAS: Thermochemical interactions and mitigation approaches. *Journal of Thermal Spray Technology*, 19:156–167, 2010.

[57] C. E. Murray. Equivalence of Kröner and weighted Voigt-Reuss models for x-ray stress determination. *Journal of Applied Physics*, 113:153509, 2013.

[58] J. Nicholls, M. Deakin, and D. Rickerby. A comparison between the erosion behaviour of thermal spray and EB-PVD deposition TBC. *Elsevier Science S.A.*, 233-235:352–361, 1999.

[59] I. Noyan and J. Cohen. *Residual Stress*. Springer-Verlag, 1987.

[60] J. Nychka, D. R. Clarke, S. Sridharan, E. Jordan, M. Gell, M. J. Lance, C. J. Chunnilalld, I. M. Smith, S. R. J. Saunders, R. Pillan, V. Sergo, A. Selcuk, A. Atkinson, and K. S. Murphy. NDE assessment of TBCs: an interim report of a photo-stimulated luminescence round-robin test. *Surface and Coatings Technology*, 163-164:87–94, 2003.

[61] J. A. Nychka and D. R. Clarke. Damage quantification in TBCs by photo-stimulated luminescence spectroscopy. *Surface Coatings and Technology*, 146-147:110–116, 2001.

[62] N. P. Padture, M. Gell, and E. H. Jordan. Thermal barrier coatings for gas-turbine engine applications. *Science*, 296:280–284, 2002.

[63] P. Patnaik, X. Huang, and J. Singh. State of the art and future trends in the development of thermal barrier coating systems. *Innovative Missile Systems*, pages 38–1–38–20, 2006.

[64] X. Peng and D. R. Clarke. Piezospectroscopic analysis of interface debonding in thermal barrier coatings. *Journal of American Ceramic Society*, 83:1165–1170, 2000.

[65] S. Raghavan, P. Imbrie, and W. Crossley. The spectral analysis of R lines and vibronic sidebands in the emission spectrum of ruby using genetic algorithms. *Applied Spectroscopy*, 62:759–765, 2008.

[66] K. W. Schlichting, N. P. Padture, E. H. Jordan, and M. Gell. Failure modes in plasma-sprayed thermal barrier coatings. *Materials Science and Engineering A*, 342:120–130, 2003.

[67] K. W. Schlichting, K. Vaidyanathan, Y. H. Sohn, E. H. Jordan, M. Gell, and N. P. Padture. Application of Cr^{3+} photoluminescence piezo-spectroscopy to plasma-sprayed thermal barrier coatings for residual stress measurement. *Materials Science and Engineering A*, 291(1-2):68–77, 2000.

[68] J. Schwarzer, D. Lohe, and O. Vohringer. Influence of the TGO creep behavior on delamination stress development in thermal barrier coating systems. *Materials Science and Engineering A*, 387-389:692–695, 2004.

[69] A. Selcuk and A. Atkinson. Analysis of the Cr^{3+} luminescence spectra from thermally grown oxide in thermal barrier coatings. *Materials Science and Engineering A*, A335:147–156, 2002.

[70] E. A. G. Shillington and D. R. Clarke. Spalling failure of a thermal barrier coating associated with aluminum depletion in the bond-coat. *Acta Materialia*, 47:1297–1305, 1999.

[71] S. F. Siddiqui, K. Knipe, A. Manero, C. Meid, J. Wischek, J. Okasinski, J. Almer, A. M. Karlsson, M. Bartsch, and S. Raghavan. Synchrotron x-ray measurement techniques for thermal barrier coated cylindrical samples under thermal gradients. *Review of Scientific Instruments*, 84:083904, 2013.

[72] M. Song, Y. Ma, and S. kai Gong. Analysis of residual stress distribution along interface asperity of thermal barrier coating system on macro curved surface. *Progress in Natural Science: Materials International*, 21(3):262–267, 2011.

[73] S. Sridharan, L. Xie, E. H. Jordan, and M. Gell. Stress variation with thermal cycling in the thermally grown oxide of an EB-PVD thermal barrier coating. *Surface Coatings and Technology*, 179:286–296, 2004.

[74] M. Tanaka, R. Kitazawa, T. Tomimatsu, Y. Liu, and Y. Kagawa. Residual stress measurement of an EB-PVD $Y_2O_3 - ZrO_2$ thermal barrier coating by micro-raman spectroscopy. *Surface & Coatings Technology*, 204:657–660, 2009.

[75] M. Tanaka, Y. Liu, and Y. Kagawa. Identification of delamination through TGO stresses due to indentation testing of an EB-PVD TBC. *J. Mater. Res.*, 24 No. 12:3533–3542, 2009.

[76] T. A. Taylor. US Patent No. 5,073,433, 1991.

[77] T. A. Taylor, D. L. Appleby, A. Bolcavage, A. Feuerstein, and N. Hitchman. Dense vertically cracked thermal barrier coatings, 2012.

[78] J. Thornton, S. Slater, and J. Almer. The measurement of residual strains within thermal barrier coatings using high-energy x-ray diffraction. *Journal of the American Ceramic Society*, 88:2817–2825, 2005.

[79] T. Tomimatsu, Y. Kagawa, and D. R. Clarke. Determination of the R-line luminescence spatial resolution of a near-field optical spectroscopy system for piezospectroscopy. *Journal of Applied Physics*, 101:123527–1–123527–8, 2007.

[80] T. Tomimatsu, Y. Kagawa, and S. Zhu. Residual stress distribution in electron beam-physical vapor deposited ZrO_2 thermal barrier coating layer by Raman spectroscopy. *Metallurgical And Materials Transactions A*, 34A:1739–1741, 2003.

[81] T. Tomimatsu, S. Zhu, and Y. Kagawa. Effect of thermal exposure on stress distribution in TGO layer of EB-PVD TBC. *Acta Materialia*, 51(8):2397–2405, 2003.

[82] T. Tomimatsu, S. Zhu, and Y. Kagawa. Local stress distribution in thermally-grown-oxide layer by near-field optical microscopy. *Scripta Materialia*, 50:137–141, 2004.

[83] L. Wang, Y. X. Zhao, X. H. Zhong, S. Y. Tao, W. Zhang, and Y. Wang. Influence of "island-like" oxides on the bond-coat on the stress and failure patterns of the thermal-barrier coatings fabricated by atmospheric plasma spraying during long-term high temperature oxidation. *Journal of Thermal Spray Technology*, 23(3):431–446, 2014.

[84] R. Wellman, G. Whitman, and J. Nicholls. CMAS corrosion of EB PVD TBCs: Identifying the minimum level to initiate damage. *Int. Journal of Refractory Metals & Hard Materials*, 28:124–132, 2010.

[85] P. K. Wright and A. G. Evans. Mechanisms governing the performance of thermal barrier coatings. *Current Opinion in Solid State and Materials Science*, 4:255–265, 1999.

[86] H. Yu and D. R. Clarke. Effect of codoping on the R-line luminescence of Cr^{3+}-doped alumina. *Journal of American Ceramic Society*, 85(8):1966–1970, 2002.

[87] S. Zhu, K. Fukuda, and T. Osaki. Residual stress in TGO and interfacial damage in thermal barrier coating after thermal exposure and cyclic indentation. *Journal of Solid Mechanics and Materials Engineering*, 4 No. 2:244–251, 2010.